Title

Mathematical modeling of depressive disorders: Circadian driving, bistability and dynamical transitions.

Authors

Cheng, Xiaoou
DOrsogna, Maria
Chou, Tom

Publication Date

2021

DOI

10.1016/j.csbj.2020.10.035

Computational and Structural Biotechnology Journal 19 (2021) 664–690

ELSEVIER

COMPUTATIONAL ANDSTRUCTURAL BIOTECHNOLOGY JOURNAL

journal homepage: www.elsevier.com/locate/csbj

Mathematical modeling of depressive disorders: Circadian driving, bistability and dynamical transitions

Xiaoou Cheng [a], Maria R. D'Orsogna [b,c], Tom Chou [c,d]

[a] School of Mathematical Sciences, Peking University, Haidian District, Beijing 100871, China
[b] Dept. of Mathematics, California State University, Northridge, CA 91330, United States
[c] Dept. of Computational Medicine, UCLA, Los Angeles, CA 90095, United States
[d] Dept. of Mathematics, UCLA, Los Angeles, CA 90095, United States

ARTICLE INFO

Article history:
Received 18 August 2020
Received in revised form 30 October 2020
Accepted 30 October 2020
Available online 21 November 2020

Keywords:
Dynamical systems
Circadian rhythm
Depressive disorders
PTSD
Chaos
Bistability
Cognitive behavioral therapy

ABSTRACT

The hypothalamus–pituitary–adrenal (HPA) axis is a key neuroendocrine system implicated in stress response, major depression disorder, and post-traumatic stress disorder. We present a new, compact dynamical systems model for the response of the HPA axis to external stimuli, representing stressors or therapeutic intervention, in the presence of a circadian input. Our work builds upon previous HPA axis models where hormonal dynamics are separated into slow and fast components. Several simplifications allow us to derive an effective model of two equations, similar to a multiplicative-input FitzHugh-Nagumo system, where two stable states, a healthy and a diseased one, arise. We analyze the effective model in the context of state transitions driven by external shocks to the hypothalamus, but also modulated by circadian rhythms. Our analyses provide mechanistic insight into the effects of the circadian cycle on input driven transitions of the HPA axis and suggest a circadian influence on exposure or cognitive behavioral therapy in depression, or post-traumatic stress disorder treatment.

1. Introduction

When presented with external stimuli and challenges, organisms activate a series of physiological and behavioral actions to minimize departure from homeostasis. These body-brain responses are mostly coordinated by the hypothalamic–pituitary–adrenal (HPA) axis which controls the expression of three major stress-related hormones: CRH (corticotropin-releasing hormone), ACTH (adrenocorticotropic hormone), and glucocorticoids, through a complex set of interactions, ligand-receptor binding events, and feedback loops [1,2]. The most prevalent glucocorticoid in humans is cortisol. The above hormones are secreted on a circadian basis: under normal conditions levels are low at night, peak in the early morning hours and decline slowly throughout the day [3]. Non-stimulated basal CRH is released in a pulsatile manner with a frequency of about two to three episodes per hour; similarly ACTH and cortisol manifest burst-like releases that follow a 60–90 min periodicity [4–9]. As a result, an ultradian rhythm is superimposed on the circadian cycle of each hormone. Animal studies suggest that pulsatile CRH is not the source of the ultradian ACTH and cortisol rhythms[10]. On the other hand, ACTH and cortisol pulses are highly correlated, with cortisol typically trailing ACTH by a 15-min delay [11].

The HPA axis regulates many physiological processes, including digestion, the immune system, mood and emotions, sexuality and metabolism. It is a highly conserved system that is present in many vertebrate, invertebrate and mono-cellular species. Due to its central role in the body's response to environmental stimuli and demands, disruptions to the HPA axis and related neuroendocrine activity are associated to a wide variety of pathologies, including stress-related ones [12]. For example, over-production of CRH may be linked to major depressive disorder (MDD) [13–17] and to anorexia nervosa where hypercortisolemia is also observed [18–20]. Patients with acute MDD have also reported elevated cortisol levels [21]. Increased ACTH and/or cortisol levels are observed in patients with Nelson's syndrome, Cushing syndrome or Cushing disease [22–25]. Cortisol production irregularities are also linked to Sheehan's syndrome and are often observed in patients with pituitary tumors [26–28]. Those at risk for depression have been found to exhibit greater waking cortisol and a larger cortisol awakening response [29], while abnormally low cortisol levels are observed in post-traumatic stress disorder (PTSD) patients as measured by urinary and/or salivary samples [30–39]. Addison disease,

https://doi.org/10.1016/j.csbj.2020.10.035
2001-0370/© 2020 The Author(s). Published by Elsevier B.V. on behalf of Research Network of Computational and Structural Biotechnology.

or primary adrenal insufficiency, is marked by low levels of cortisol due to adrenal gland disorders; secondary adrenal insufficiency is marked by low levels of ACTH and cortisol due to dysregulation of the pituitary gland; tertiary adrenal insufficiency is marked by low levels of CRH, ACTH, and cortisol, due to hypothalamic diseases [40]. Addison disease may also be characterized by high levels of ACTH. Here, since the adrenal cortex is unable to synthesize and/or secrete cortisol, the pituitary gland increases production of ACTH in an effort to stimulate it. Some studies associate elevated levels of CRH and cortisol to the onset of dementia and Alzheimer's disease, whereas others observe low CRH concentrations in patients with advanced neurodegenerative conditions [41]. These seemingly contrasting findings may be due to chronic HPA axis overstimulation, where high levels of CRH and cortisol may induce permanent damage to neuronal connectivity, so that eventually secretion of CRH is reduced [42]. Other contradictory findings may emerge in surveying the literature on alterations to HPA-regulated hormonal activity. For example not all studies report cortisol deficiencies [43] among PTSD patients. These discrepancies may be due to methodological variabilities in sampling and/or timing, limited number of participants, confounding effects such as patients of different ages or who are taking medications that affect hormonal expression, and other extraneous factors.

As described above, one of the most important functions of the HPA axis is to maintain homeostasis in response to mild to severe stress via the enhanced release of CRH from the hypothalamus, initiating the CRH–ACTH–cortisol cascade. The secretion of cortisol helps the body cope with the stressor, for example by facilitating the release of glucose to activate "fight or flight" responses. However, sometimes the trauma is so severe (or the individual experiencing it is particularly susceptible) that the normal HPA axis response is disrupted and abnormal levels of stress hormones are produced on a permanent basis. Thus, acute stressful events such as major accidents, combat, assaults, natural disasters, death of a loved one, can lead to neuroendocrine dysfunction. This happens in PTSD and in MDD: both can be triggered by episodes of acute stress, and are characterized by abnormally low cortisol levels (one biomarker of PTSD) and over-expression of CRH (a biomarker of MDD). The evidence that the HPA axis is hypo/hyper active in PTSD and/or MDD comes from clinical trials, biochemical studies, functional HPA axis tests, neuro-imaging and postmortem studies. Based on these observations, we formulate our main modeling assumption, that external stressors may cause long-lasting damage.

The neuroendocrine dynamics of the HPA axis has been well-studied using mathematical models that describe the abundances of CRH, ACTH, cortisol, and glucocorticoid receptors and their dynamics in response to external inputs [44–56]. These models include physiologically motivated feedback loops and delays that allow for the emergence of the ultradian oscillations. The external input, which may be time dependent, is interpreted as environmental stimulus, stressor or trauma, while the circadian rhythm is typically neglected. Under given parametric regimes and modeling conditions two stable states or limit cycles emerge: one is identified as the "healthy" or "healthy" state, the other as a psychiatrically "perturbed" or "diseased" condition [47,49]. Transitions between the two states may arise from parameter changes, which we interpret as physical injury, or as a function of external input, which we interpret as psychological trauma. In the latter case, HPA stress-related disorders may be viewed as a consequence of the bistability of the system, with the diseased state emerging as an organism's response to psychological stress, rather than to physiological damage. Mood disorders often appear as abnormalities in CRH expression, which also manifest downstream, in ACTH and/or cortisol expression. We thus seek for bistability at the origin of the hormonal sequence that is regulated by the HPA axis, that is at the CRH level.

Separating CRH dynamics into a fast CRH release and a slow CRH synthesis yields a larger parameter space and higher likelihood for the emergence of the healthy-diseased bistable configuration [55,56]. Apart from the action of external stressors, the time-varying input into the hypothalamus can also model cognitive behavioral therapy (CBT) or exposure therapy (ET), where patients are subjected to psychological interventions or exposed to the stressor in a controlled manner to relieve them of depression, PTSD and other stress related symptoms. Within these dynamical systems models, external inputs can trigger transitions between the healthy and diseased states depending on input duration, amplitude and time of application relative to the intrinsic oscillations of the ultradian cortisol pulses [55,56].

The circadian cycle, which is known to affect the regulation and metabolism of several hormones, has been neglected in previous mathematical analyses. Here, we incorporate it as an input to the dynamical system. Physiologically, the relevant oscillating pacemaker is located in the suprachiasmatic nucleus (SCN), a group of neurons in the hypothalamus that respond to photosensitive ganglion cells in the retina [57–59]. The circadian rhythm can modulate input from the hypothalamus to stimulate the secretion of CRH hormones in the portal vessel which connects the hypothalamus to the anterior pituitary [60]; it may also cause oscillations in the relevant tissues and organs that comprise the HPA axis and that respond to the SCN independently of the hypothalamus.

In Section 2, we derive a dynamical systems model of the HPA axis. The "fundamental" form we present in Eqs. 12 and 13 is based on existing models but it is more mathematically compact, allowing us to better study the parameter regimes that yield healthy-diseased bistability, and to include circadian driving. In Section 3 we discuss how the circadian driving affects the dynamics and equilibria of the fundamental form, through analytical and numerical analysis. In Section 4 we include various forms of external inputs representing trauma and/or exposure therapy. The complete stimulus to the HPA axis is given by the superposition of basal, rhythmic and external/reactive terms. We show that the magnitude and duration of the external input, its timing relative to the phase of the circadian cycle, and the amplitude of the circadian rhythm, strongly affect the transition between healthy and diseased states. We offer conclusions and a brief discussion in Section 5.

2. Reduced model without circadian drive

The model we use in this paper is a compact, reduced description of the HPA neuroendocrine system that is derived from previous work [53,49,54,48,50–52,55,56]. The simplifications introduced allow us to incorporate the circadian drive and perform complete analytical analyses. We begin by illustrating the full, initial model which includes five variables that represent the most relevant hormones and receptors involved in stress response [55,56]. Later we show how our new, compact two-variable system is obtained.

The CRH neurons are the first to be activated by physiological changes such as stress and the HPA axis model we consider includes two compartments for it. One is CRH storage, that obeys relatively slow dynamics, on the order of ten to twelve hours; the other is CRH secretion, that follows relatively fast dynamics, on the order of minutes. Secreted CRH initiates a cascade of events that includes ACTH and cortisol production. Feedback loops emerge from circulating cortisol binding to glucocorticoid receptors leading to inhibition of ACTH and self-upregulation of glucocorticoid receptor production. Depending on the parameters chosen, a maximum of two stable fixed points may arise, which are interpreted as the healthy and diseased states. Specific time-dependent perturbations of the external input into the hypothalamus can drive transitions from one stable point to the other, suggesting that onset of dysfunction in stress response and its treatment can be framed in terms of dynamical bistability. In non-dimensional terms, the full model [55,56] is given by

$$\begin{cases} \dfrac{\mathrm{d}c_s(t)}{\mathrm{d}t} = \dfrac{c_\infty(o) - c_s}{t_c}, \\ \dfrac{\mathrm{d}c(t)}{\mathrm{d}t} = q_0 I(t)(1 - \mathrm{e}^{-kc_s}) + g_{c,\max}\dfrac{(q_1 c)^n}{1 + (q_1 c)^n} - q_2 c, \\ \dfrac{\mathrm{d}a(t)}{\mathrm{d}t} = \dfrac{c}{1 + p_2(or)} - p_3 a, \\ \dfrac{\mathrm{d}o(t)}{\mathrm{d}t} = a - o, \\ \dfrac{\mathrm{d}r(t)}{\mathrm{d}t} = \dfrac{(or)^2}{p_4 + (or)^2} + p_5 - p_6 r. \end{cases} \tag{1}$$

Here, $c_s(t)$ represents the slowly evolving concentration of stored CRH in the neurons of the paraventricular nucleus of the hypothalamus, which is not directly affected by the external input, but rather depends on circulating cortisol. Stored CRH may be quickly released into the hypophyseal portal vessels before being transported to the anterior pituitary. The concentration of CRH in this "circulating" pool is denoted $c(t)$. The stored CRH concentration $c_s(t)$ evolves on the long time scale t_c and relaxes towards an equilibrium value $c_\infty(o)$ that depends on cortisol levels o through an indirect negative feedback process. From experimental observations on rats $c_\infty(o) = \bar{c}_\infty + \mathrm{e}^{-bo}$ so that at steady state the stored $c_s(t)$ decreases with $o(t)$, leveling at $\bar{c}_\infty$ for large cortisol levels as modulated by the parameter b [61,62]. Aside from natural degradation modeled by the $-q_2 c$ term, the dynamics of $c(t)$ is driven by two processes. The first is the stimulus $I(t)$ that triggers release of stored CRH: this is modeled by the product between $I(t)$ and $q_0(1 - \mathrm{e}^{-kc_s(t)})$. In this expression q_0 is the maximum possible secretion rate of the stored c_s pool to the circulating CRH pool which is achieved in the $c_s \to \infty$ limit. For $c_s \to 0$, there is no stored CRH to release. The coefficient k modulates the response between these two limits. The second process is self-upregulation, whereby circulating CRH stimulates further release of the same hormone [62]. Since upregulation is mediated by CRH/receptor binding, we use a Hill-type increasing function that varies between 0 and $g_{c,\max}$. The coefficient q_1 is the inverse of the CRH concentration that produces half maximum self-upregulation, and the Hill coefficients used are $n = 5$, although other choices of n will not qualitatively change our results. The concentration of ACTH generated in the pituitary gland is denoted as a. As can be seen from Eqs. 1, its production is driven by circulating c levels but inhibited by cortisol o bound to glucocorticoid receptors r through the negative feedback term $(1 + p_2(or))^{-1}$. ACTH is cleared at rate p_3. Cortisol production in the adrenal gland is driven by $a(t)$ and follows a natural decay. Finally, glucocorticoid receptors in the anterior pituitary self-upregulate through cortisol binding to the receptors themselves [63]. The dynamics of r thus assumes a cortisol-independent production rate p_5 and cortisol-mediated generation represented by the $(or)^2/(p_4 + (or)^2)$ term; the clearance rate is p_6. The non-dimensional parameters in Eqs. 1 are highly variable and may depend on genetic traits, age, gender, and other environmental factors. Parameter choices are important as they may (or may not) lead to bistable solutions, representing individuals who are less (or more) resistant to dysfunctions of the HPA axis. The parameters we use in this work for Eqs. 1 lead to bistability. They are set as in [56], and are listed in Table. 1.

Table 1

Non-dimensional parameter values of the model Eqs. 1 as taken from Refs. [55,56]. We also include non-dimensional parameter values for the 24-h circadian rhythm.

Parameter	Value	Description
$\bar{c}_\infty$	0.2	minimal stored baseline CRH
b	0.6	stored CRH decay as a function of cortisol
t_c	69.3	CRH biosynthesis timescale
q_0	28.0	maximum release rate of CRH in basal state
I_0	1.0	basal level of the external stimuli
k	2.83	relates stored CRH to CRH release rate
$g_{c,\max}$	42.0	maximum auto/paracrine effect of CRH in the pituitary
n	5	Hill coefficient describing the self-upregulation of CRH
q_1^{-1}	25.0	circulating CRH conc. at half-maximum self-upregulation
q_2	1.8	ratio of CRH and cortisol decay rates
p_2^{-1}	0.067	*or*-complex conc. for half-maximum negative feedback
p_3	7.2	ratio of ACTH and cortisol decay rates
p_4	0.05	(*or*-complex conc)^2 at half-maximum positive feedback on r production
p_5	0.11	basal GR production rate by pituitary
p_6	2.9	ratio of GR and cortisol decay rates
ω	0.045	frequency of 24-h circadian rhythm

Note that the model presented in Eqs. 1 is non-dimensionalized using the inverse of the decay rate of cortisol as the reference time scale and various parameter combinations to obtain c, c_s, a, o, r [54–56]. Furthermore, in the original formulation of the model, a delay τ was included in the ACTH activated synthesis of cortisol so that $\mathrm{d}o(t)/\mathrm{d}t = a(t-\tau) - o(t)$ [55,56]. The delayed response of the adrenal gland to ACTH is well established and estimated to be roughly 15 min [11]. Physiologically, the delay is due to the delivery of ACTH from the pituitary to the adrenal gland and to the subsequent synthesis of cortisol. Mathematically, the delay allows for the recovery of the ultradian rhythm [54–56]. We do not consider this delay in the current work, as its mathematical implications are well understood and our goal is to understand how the circadian rhythm, which occurs on a much longer time scale than the delay, affects the dynamics. For better insight into the model, and its non-dimensionalization, the reader is referred to the analyses in [54–56].

The separation between CRH synthesis and release, processes operating on two distinct time scales, yields interesting behavior, including bistability and the possibility of transitions between the respective basins of attraction. Eqs. 1 however are mathematically cumbersome and the inclusion of a circadian rhythm would add algebraic tedium without offering clear insight. We thus present a simplified version of Eqs. 1 that exhibits the same main features but that is much simpler to analyze. To proceed, we focus only on c_s and c in Eqs. 1 and set the $\{a, o, r\}$ subsystem to equilibrium under a given c, effectively parameterizing a, o, r. We use this steady-state approximation since the $\{a, o, r\}$ subsystem evolves on a much faster timescale than c_s.

We keep the expression for c_s in Eqs. 1 and simplify the dynamics of c with the goal of preserving bistability. Henceforth, unless specified otherwise, we will work in (c_s, c) space. For a given value of $I(t) = I_0$, equilibrium is attained when the two nullclines obtained by setting $\mathrm{d}c_s/\mathrm{d}t = 0$ and $\mathrm{d}c/\mathrm{d}t = 0$ in Eqs. 1 intersect. Since they evolve on different time scales, the first, c_s-nullcline is sometimes referred to as the slow nullcline, the latter, the c-nullcline, as the fast one. Finally, note that the equilibrium values of a, o, r define single-valued, positive, real functions of c; hence, once c is specified they are uniquely defined and no bistability can emerge at this stage. Conversely, if bistability emerges in (c_s, c), space it will be reflected in (a, o, r) space as well, as parametrized by the two bistable values of c.

We begin by simplifying the right-hand side of Eqs. 1 driving the c_s dynamics. Since $c_\infty(o) = \bar{c}_\infty + \mathrm{e}^{-bo}$ we must find an explicit expression for $o(c)$ so that our new model is self-contained in (c_s, c) space. Under the assumption that the a, o, r subsystem is equilibrated, $o(c)$ can be found through algebraic manipulation of Eqs. 1 with the a, o, r derivatives set to zero so that

$$\begin{aligned}&\left[\frac{p_2p_3(1+p_5)}{p_6}(p_2^2p_3^2p_4+p_3^2)-\frac{p_4}{p_6}(p_2p_3)^3\right]o^4\\&\quad-\left[\frac{2p_2p_3^2(1+p_5)}{p_6}c-p_3^3-p_2^2p_3^3p_4\right]o^3+\\&\quad\left[\frac{p_2p_3(1+p_5)}{p_6}c^2-3p_3^2c-p_2^2p_3^2p_4c\right]o^2+3c^2p_3o-c^3=0.\end{aligned} \tag{2}$$

As written above, o is the root of a quartic polynomial where c appears as a parameter in some of the coefficients. Writing the full exact solution to Eq. 2, while possible, is cumbersome. We note however that using realistic parameters given in Refs.[55,56] the term

$$\begin{aligned}&\left[\frac{p_2p_3(1+p_5)}{p_6}(p_2^2p_3^2p_4+p_3^2)-\frac{p_4}{p_6}(p_2p_3)^3\right]o^4\\&\quad+\left[\frac{2p_2p_3^2(1+p_5)}{p_6}c-p_3^3-p_2^2p_3^3p_4\right]o^3-3c^2p_3o\end{aligned}$$

is relatively small compared to others. Thus, the relation between o and c can be approximated by adding the three above terms to Eq. 2, leading to a quadratic equation in o^2:

$$\begin{aligned}&2\left[\frac{p_2p_3(1+p_5)}{p_6}(p_2^2p_3^2p_4+p_3^2)-\frac{p_4}{p_6}(p_2p_3)^3\right]o^4\\&\quad+\left[\frac{p_2p_3(1+p_5)c^2}{p_6}-3p_3^2c-p_2^2p_3^2p_4c\right]o^2 \;=\; c^3.\end{aligned} \tag{3}$$

This simplified quadratic equation can be solved for $o^2(c)$ and the resulting $o(c)$ can be inserted into $c_\infty(o)=\bar{c}_\infty+\mathrm{e}^{-bo}$ in the first of Eqs. 1 so that the evolution of $c_s(t)$ is completely described in (c_s,c) space. The approximated and full-model $o(c)$ are shown in Fig. 1. In Appendix 6 we discuss further approximations to the term $\mathrm{e}^{-bo(c)}$ in Eqs. 1.

We now explore approximations to the c dynamics in the second of Eqs. 1 which couples c_s and c. The analytical work in Ref. [55,56] reveals that the key to bistability is the sigmoid, "S" shape of the c-nullcline. Since the cubic is one of the simplest forms to yield a sigmoid shape, we tailor an ad hoc cubic function $c_s(c)$ as a proxy for the c-nullcline. To do this in a consistent manner, certain conditions must be met. We first consider the case of a fixed input, $I(t)=I_0$. As can be seen in [55,56] increasing I_0 will shift the c-nullcline to the left in (c_s,c) space; also the c-loci of the turning points of the c-nullcline are mostly insensitive to I_0. The c-nullcline must also pass through the origin so that if no CRH is synthesized, no CRH can be released. Similarly, $\mathrm{d}c/\mathrm{d}t>0$when $c_s>0$ and $c=0$, indicating that the release of CRH increases when stored, synthesized CRH is present. We also impose that $\mathrm{d}c/\mathrm{d}t<0$when $c_s=0$ and $c>0$ so that when there is no stored CRH present, no CRH can be released and its concentration c will decrease due to degradation. We thus posit $\mathrm{d}c/\mathrm{d}t=k_2I_0c_s-k_1f(c)$ where $f(c)$ is a cubic in c with $f(0)=0$ and $f(c)>0$ for $c>0$. The proportionality constant k_2 should be positive so that $c_s>0, c=0$ values will yield $\mathrm{d}c/\mathrm{d}t>0$. Furthermore, to preserve positivity along the c-nullcline, $c_s=k_1f(c)/k_2I_0$, we must also impose that $k_1>0$; positive values of k_1 also guarantee that if $c_s=0, c>0$ then $\mathrm{d}c/\mathrm{d}t<0$, as discussed above. Typical values of c are one order of magnitude larger than those of c_s [55,56]; as a result k_1 must be much smaller than k_2, so that the nullcline equation $c_s=k_1f(c)/k_2I_0$, which includes a cubic in c, will yield reasonable values of c_s. Under the assumption $k_1\ll k_2$, we finally write

$$\frac{\mathrm{d}c}{\mathrm{d}t} \;=\; k_2I_0c_s-k_1\left(\frac{c^3}{3}-\frac{c_1^*+c_2^*}{2}c^2+c_1^*c_2^*c\right), \tag{4}$$

so that increases in I_0 shift the nullcline to the left in (c_s,c) space as imposed above. The quantities $c_{1,2}^*$ represent the turning points of the cubic defined by $f(c)=c^3/3-(c_1^*+c_2^*)/2c^2+c_1^*c_2^*c$, so that $\mathrm{d}f(c_{1,2}^*)/\mathrm{d}c=0$. Without loss of generality we assume $0<c_1^*<c_2^*$. Since c_s must be positive at the $c=c_{1,2}^*$ turning points, we must also impose $c_2^*>c_1^*/3$ and $c_1^*>c_2^*/3$. The form of the right-hand-side of Eq. 4 implies that the c-nullcline follows a sigmoidal "S" shape where the c-coordinate of the turning points are independent of I_0 as desired.

We can arrive at a similar expression for Eq. 4 through a different route. Performing a Taylor expansion in c_s of the right-hand side of the c dynamics in Eqs. 1, the term $q_0I_0(1-\mathrm{e}^{-kc_s})$ yields $q_0kI_0c_s$ to first order, whereas the expansion in $(q_1c)^n$ of $g_{c,\max}(q_1c)^n/(1+(q_1c)^n)$ results in $g_{c,\max}\left[(q_1c)^n-(q_1c)^{2n}\right]$ to second order so that setting $n=3/2$ yields a cubic term with a negative coefficient. Upon including a time-dependent form for $I(t)$, the substitution $I_0\to I(t)$ will shift the c-nullcline accordingly. The full model can thus be re-written as

$$\frac{\mathrm{d}c_s}{\mathrm{d}t} \;=\; \frac{\bar{c}_\infty+\mathrm{e}^{-bo(c)}-c_s}{t_c}, \tag{5}$$

$$\frac{\mathrm{d}c}{\mathrm{d}t} \;=\; k_2I_0c_s-k_1\left(\frac{1}{3}c^3-\frac{c_1^*+c_2^*}{2}c^2+c_1^*c_2^*c\right). \tag{6}$$

where $o(c)$ is the approximated form given implicitly in Eq. 3, and where time-dependent inputs $I(t)$ can be easily incorporated in lieu of I_0. To guarantee bistability, the c_s and the c nullclines must allow for multiple intersections. Let us denote the coordinates of the turning points of the cubic on the c-nullcline as $(c_{s,1}^*,c_1^*)$ and $(c_{s,2}^*,c_2^*)$, where $c_{s,1}^*=k_1f(c_1^*)/k_2I_0$ and $c_{s,2}^*=k_1f(c_2^*)/k_2I_0$ with $c_1^*<c_2^*$. Since c decreases along the slow nullcline as c_s increases, multiple crossings of the two nullclines will arise if $(c_{s,1}^*,c_1^*)$ lies to the right of the slow, c_s nullcline, and $(c_{s,2}^*,c_2^*)$ lies to its left. Mathematically this is translated into the following bistability condition

$$c_{s,1}^* > \bar{c}_\infty+\mathrm{e}^{-bo(c_1^*)}, \tag{7}$$

$$c_{s,2}^* < \bar{c}_\infty+\mathrm{e}^{-bo(c_2^*)}. \tag{8}$$

As discussed above, c is typically one order of magnitude larger than c_s [55,56]. We thus further rescale c_s by a factor $\kappa=(k_2/k_1)\gg 1$ so that the two CRH components are comparable in size and define

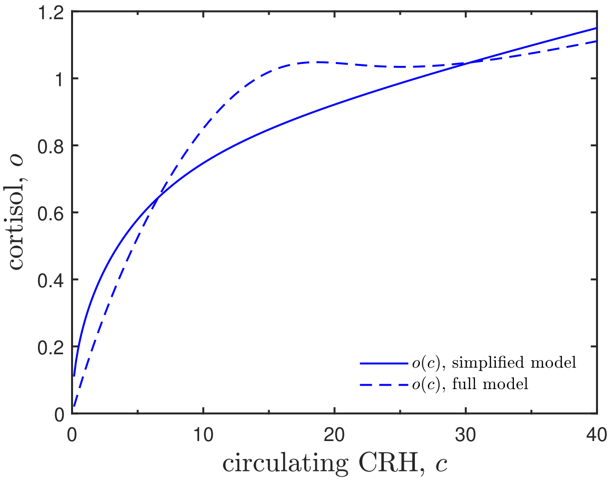

Fig. 1. The $o(c)$ curve expressing cortisol as a function of circulating CRH from the full model is plotted by solving the exact Eq. 2 and is shown as a dashed line. The $o(c)$ curve from the simplified model derived from the approximate Eq. 3 is shown as a solid line. Henceforth we will use the latter as it allows for an analytical solution, while preserving the scale and salient features of the full model $o(c)$. In both cases parameters from Table 1 are used.

$$x = c_s, \tag{9}$$

$$y = c\left(\frac{k_1}{k_2}\right)^{1/3} = \frac{c}{\kappa^{1/3}}, \tag{10}$$

$$t' = tk_1^{1/3}k_2^{2/3}. \tag{11}$$

Note that the rescaling will also affect the time scale t, as seen from Eq. 11. For simplicity, we drop the prime notation from t' and introduce $\varepsilon = 1/(t_c k_1^{1/3} k_2^{2/3})$. Since the dynamics of c_s unfolds on the longer time scale t_c compared to that of c, we also assume $t_c^3 \gg k_1^{-1}k_2^{-2}$ so that $\varepsilon \ll 1$. Our reduced model is now complete. The ODE system written in terms of (x, y) is given by

$$\frac{\mathrm{d}x}{\mathrm{d}t} = \varepsilon(\bar{c}_\infty + \mathrm{e}^{-bo(y)} - x), \tag{12}$$

$$\frac{\mathrm{d}y}{\mathrm{d}t} = I_0 x - \left(\frac{1}{3}y^3 - \frac{y_1^* + y_2^*}{2}y^2 + y_1^* y_2^* y\right), \tag{13}$$

where $o(y)$ is the real, positive solution to

$$\begin{aligned} &2\left[\frac{p_2p_3(1+p_5)}{p_6}(p_2^2p_3^2p_4 + p_3^2) - \frac{p_4}{p_6}(p_2p_3)^3\right]o^4 \\ &+\left[\frac{p_2p_3(1+p_5)}{p_6}\kappa^{\frac{2}{3}}y^2 - 3p_3^2\kappa^{\frac{1}{3}}y - p_2^2p_3^2p_4\kappa^{\frac{1}{3}}y\right]o^2 - \kappa y^3 = 0, \end{aligned} \tag{14}$$

and $y_{1,2}^*$ are the rescaled $c_{1,2}^*$ values according to Eq. 10 and subject to the following constraints

$$y_1^* > y_2^*/3 > 0 \qquad x_1^* = \frac{3{y_1^*}^2 y_2^* - {y_1^*}^3}{6I_0} > \bar{c}_\infty + \mathrm{e}^{-bo(y_1^*)}, \tag{15}$$

$$y_2^* > y_1^*/3 > 0 \qquad x_2^* = \frac{3{y_2^*}^2 y_1^* - {y_2^*}^3}{6I_0} < \bar{c}_\infty + \mathrm{e}^{-bo(y_2^*)}. \tag{16}$$

The form of our reduced model in Eqs. 12 and 13 under the constraints given by Eqs. 15 and 16 is reminiscent of that of the FitzHugh-Nagumo model for neuron spiking [64], which exhibits rich dynamics in response to external excitations such as graded responses, the appearance and disappearance of limit cycles, and large excursions in phase space depending on the amplitude of the external input. In Fig. 2 we show the area in (y_1^*, y_2^*) parameter space that yields bistability (*i.e.* two stable equilibria) obtained by taking into account all constraints, Eqs. 15 and 16 and the assumption that $y_1^* < y_2^*$. For given y_1^*, y_2^* values selected from this region, the corresponding x_1^*, x_2^* values can be calculated through Eqs. 15 and 16, leading to (x_1^*, y_1^*) and (x_2^*, y_2^*) coordinates for the turning points of the cubic term in the fast y-nullcline.

Once all the physiological parameters are chosen, transitions between the two stable equilibria can be induced by perturbations, even transient ones, to the stimulus $I(t)$. In principle, one can consider a more complex description of the system where instead of bistability, the nullclines intersect three or more times. Two of these equilibria would then represent healthy and diseased conditions, the others would be interpreted as prenosological states. Mental disorders in combatants for example can be preceded by milder neurotic conditions [65]. In this case, changes to $I(t)$ could induce direct transitions between healthy and diseased states, but could also modulate a first passage from the healthy to the prenosological state, and then from the prenosological to the diseased state. Another scenario is that of a tailored $I(t)$ that once the prenosological state is reached would lead to a reverse transition back to the healthy one, representing early intervention. For simplicity we only consider bistability in the remainder of this paper.

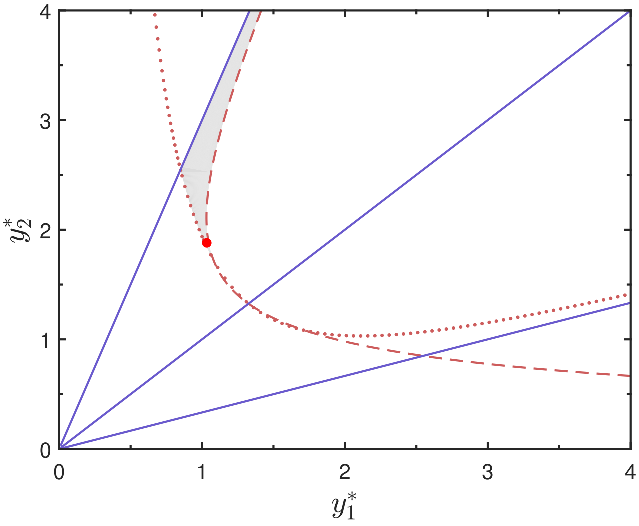

Fig. 2. Shaded in gray is the parameter region in (y_1^*, y_2^*) space that yields bistability for $\kappa = \frac{1}{3} \times 10^4$. The constraints that lead to this region are detailed in the text. The three blue lines are $y_2^* = 3y_1^*, y_2^* = y_1^*$ and $y_2^* = \frac{1}{3}y_1^*$. The dotted curve is implicitly defined via $x_1^* = \bar{c}_\infty + \mathrm{e}^{-bo(y_1^*)}$; the dashed one via $x_2^* = \bar{c}_\infty + \mathrm{e}^{-bo(y_2^*)}$ as in Eqs. 15 and 16 respectively, with $I_0 = 1$. All other parameters are as listed in Table 1. We set $y_1^* = 1.04, y_2^* = 1.87$ as denoted by the red dot. These values fall in the bistable, gray region and allow for good qualitative agreement between Eqs. 12 and 13, and the full model in Eqs. 1.

2.1. Analysis of the dynamical model without circadian drive

The steady-state solutions $(x_\mathrm{u}, y_\mathrm{u})$ of the reduced model Eqs. 12 and 13 are found by setting their right-hand sides to zero so that

$$x_\mathrm{u} = \bar{c}_\infty + \mathrm{e}^{-bo(y_\mathrm{u})}, \tag{17}$$

$$I_0 x_\mathrm{u} = \frac{1}{3}y_\mathrm{u}^3 - \frac{y_1^* + y_2^*}{2}y_\mathrm{u}^2 + y_1^* y_2^* y_\mathrm{u}. \tag{18}$$

If the turning point coordinates $y_{1,2}^*$ are chosen as in Fig. 2, two distinct solutions arise and $(x_\mathrm{u}, y_\mathrm{u}) = (x_+, y_+)$ or (x_-, y_-), labelled according to $x_+ > x_-$. In Fig. 3 we compare the nullclines derived from Eqs. 12 and 13 with those arising from the full model in Eqs. 1, showing that qualitative features are preserved. Two differ-

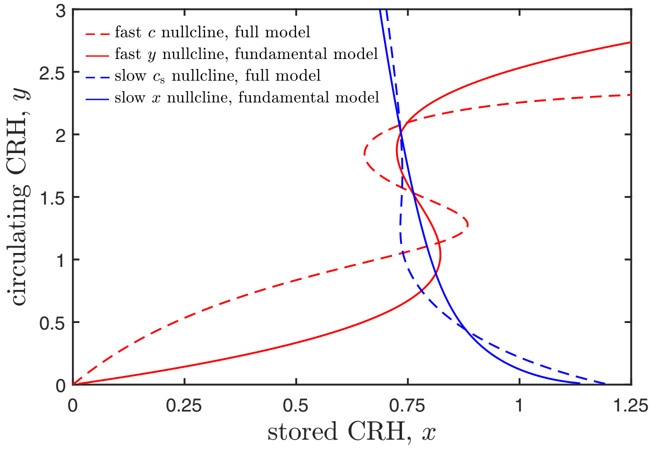

Fig. 3. Fast CRH release (solid, red) and slow CRH synthesis (solid, blue) nullclines of the fundamental HPA axis model obtained by setting $dx/dt = 0$ and $dy/dt = 0$ respectively in Eqs. 12 and 13. For comparison we also plot the corresponding c-nullcline (dashed, red) and c_s-nullcline (dashed, blue) from Eqs. 1 as a function of $x = c_s$ and $y = c/\kappa^{1/3}$. Although the details of the nullclines from the model (Eqs. 12 and 13) and from the full model (Eqs. 1) differ, the main features persist. All parameters used are as in Table 1.

ent ways for the equilibrium values to relate to each other are shown in Fig. 4. To the left, the stable points are characterized by $x_+ > x_-$ and $y_+ < y_-$; to the right $x_+ > x_-$ and $y_+ > y_-$. When identifying healthy and diseased states with either of the two $(x_\mathrm{u}, y_\mathrm{u})$ equilibria, the relation between y_+, y_- will be important since, as discussed in the Introduction, stored CRH (a decreasing function of cortisol) and circulating CRH may be both over- or under-expressed, or one may be deficient while the other is produced in excess. The left-hand panel represents the case where abnormalities are marked by high stored CRH and low circulating CRH (or vice versa); the right-hand panel represents the case where abnormalities manifest via both high (or both low) stored and circulating CRH. We will mostly focus on the left-hand side representation but our analysis and conclusions are similarly applicable to the right-hand panel.

We can further analyze Eqs. 12 and 13 by noting that the dynamics contains two time scales: t, over which y evolves, and $\tau = \varepsilon t \ll t$ over which x evolves. To make analytical progress we use asymptotic expansion methods [66] by first calculating solutions in these two time scales respectively and then matching the solutions in the intermediate scale where are valid. We begin with the t time scale, and pose

$$x(t) = x_0(t) + \mathcal{O}(\varepsilon), \tag{19}$$

$$y(t) = y_0(t) + \mathcal{O}(\varepsilon). \tag{20}$$

Upon inserting Eqs. 19,20 into Eqs. 12 and 13, we find to leading order in t,

$$\frac{\mathrm{d}x_0}{\mathrm{d}t} = 0, \tag{21}$$

$$\frac{\mathrm{d}y_0}{\mathrm{d}t} = I_0 x_0 - \left(\frac{1}{3}y_0^3 - \frac{y_1^* + y_2^*}{2}y_0^2 + y_1^* y_2^* y_0\right), \tag{22}$$

which imply the fast dynamics will occur along the vertical, y axis while $x = x_{0,\mathrm{init}}$ remains constant. The slower motion instead will arise from assuming Eqs. 12 and 13 evolve over the time scale $\tau = \varepsilon t$. We thus pose

$$x(\tau) = x_1(\tau) + \mathcal{O}(\varepsilon), \tag{23}$$

$$y(\tau) = y_1(\tau) + \mathcal{O}(\varepsilon), \tag{24}$$

and use the chain rule to derive

$$\frac{\mathrm{d}x_1}{\mathrm{d}\tau} = \bar{c}_\infty + \mathrm{e}^{-bo(y_1)} - x_1 \tag{25}$$

$$\varepsilon\frac{\mathrm{d}y_1}{\mathrm{d}\tau} = \left[I_0 x_1 - \left(\frac{1}{3}y_1^3 - \frac{y_1^* + y_2^*}{2}y_1^2 + y_1^* y_2^* y_1\right)\right]. \tag{26}$$

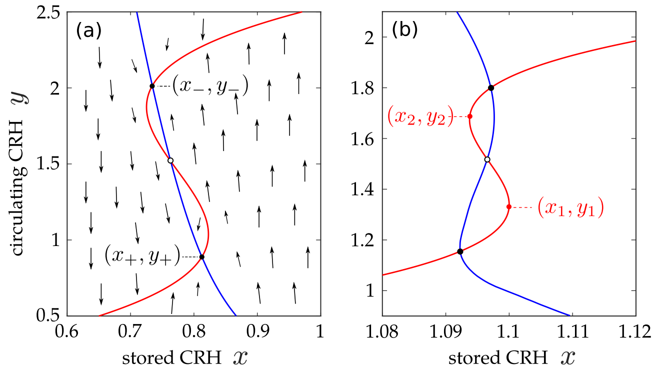

Fig. 4. Fast (red) and slow (blue) nullclines for two schematic realizations of the reduced model in Eqs. 12 and 13. (a) The slow nullcline defines a negative slope resulting in the two nullclines intersecting at equilibrium points (x_-, y_-) and (x_+, y_+), where $x_+ > x_-$ and $y_+ < y_-$. (b). The slow nullcline defines a positive slope corresponding to equilibrium points (x_-, y_-) and (x_+, y_+), where $x_+ > x_-$ and $y_+ > y_+$. In panel (a) we show the intersections $(x_\mathrm{u}, y_\mathrm{u}) = (x_\pm, y_\pm)$, in panel (b) we show the turning points (x_1, y_1) and. (x_2, y_2).

By matching orders of ε we find

$$\frac{\mathrm{d}x_1}{\mathrm{d}\tau} = \bar{c}_\infty + \mathrm{e}^{-bo(y_1)} - x_1, \tag{27}$$

$$I_0 x_1 - \left(\frac{1}{3}y_1^3 - \frac{y_1^* + y_2^*}{2}y_1^2 + y_1^* y_2^* y_1\right) = 0. \tag{28}$$

Eqs. 27 and 28 imply that over long time scales the trajectory moves along the slow nullcline, and that $x_1(\tau), y_1(\tau)$ are related via Eq. 28. The two sets of solutions, at the short and long time scales must coincide at intermediate times when $t \to +\infty$ and $\tau \to 0+$. We thus impose

$$\lim_{t\to\infty} x_0(t) = \lim_{\tau\to 0^+} x_1(\tau), \tag{29}$$

$$\lim_{t\to\infty} y_0(t) = \lim_{\tau\to 0^+} y_1(\tau). \tag{30}$$

Solving Eqs. 21 and 22 leads to $x_0(t) = x_{0,\mathrm{init}} =$ constant, while $y_0(t)$ can be found by factoring the right-hand side of Eq. 22 once $x_{0,\mathrm{init}}$ has been inserted, and solving via separation of variables. On the other hand, solving Eqs. 27 and 28 requires specifying the exact form of $o(y_1)$ which can be in principle found through Eqs. 2 or 3. However, since all functions involved are analytic and since upon inspection of Eq. 28 $y_1(\tau)$ is a function of $x_1(\tau)$, we can linearize $\mathrm{e}^{-bo(y_1)}$ as a function of x_1 and write $\mathrm{e}^{-bo(y_1)} = px_1 + q$, where $0 < px_1 + q < 1$. Under this assumption and using Eq. 29 we find

$$x_1(\tau) = \frac{\bar{c}_\infty + q}{1-p}\left[1 - \mathrm{e}^{-(1-p)\tau}\right] + x_{0,\mathrm{init}}\mathrm{e}^{-(1-p)\tau}. \tag{31}$$

We can finally estimate $y_1(\tau)$ by inserting Eq. 31 into Eq. 28 and by solving the resulting cubic equation for $y_1(\tau)$. At steady state, two stable solutions emerge for $y_1(\tau \to \infty)$ corresponding to $x_1(\tau \to \infty)$. From Eq. 31 we can also estimate the typical time scale to reach steady state as $\tau \sim 1/(1-p)$, or $t \sim 1/[(1-p)\varepsilon]$. The fully linearized problem, where we set $\mathrm{e}^{-bo(y)} = px + q$ directly into Eqs. 12 and 13, allows us to write the two nullclines as a vertical line intersecting a cubic, under fast y and slow x dynamics. We consider this problem in Appendix 6.

3. Reduced model with circadian drive

Eqs. 12 and 13 describe the fundamental dynamics of the full model without circadian driving. One important physiological feature we now add is the circadian cycle, as modulated by the SCN in the hypothalamus. This rhythm is manifest as a small, periodic variation in the basal input I_0. As a result, the full model presented in Eqs. 1 must be rewritten with a time-dependent term $I(t)$ which we model as

$$I(t) = I_0 + \alpha\sin(\omega t). \tag{32}$$

Here, α is the amplitude of the circadian perturbation, and ω its frequency, defining the period $T = 2\pi/\omega$. Since we assume the time-dependent term is small compared to the basal term, $\alpha \ll I_0$, the analysis performed in Section 2 remains valid. We can thus study our reduced problem, Eqs. 12 and 13, by replacing I_0 with $I(t)$ as expressed in Eq. 32 and with the $t \to t'$ rescaling shown in Eq. 11. Under this non-dimensionalization, $\omega t \to \omega' t'$, and the rescaled frequency is $\omega' = \omega/(k_1^{1/3}k_2^{2/3})$, corresponding to a period $T' = Tk_1^{1/3}k_2^{2/3}$ with $\omega = 2\pi/T$ given in Table 1. Henceforth we consider the rescaled version of Eq. 32, $I(t') = I_0 + \alpha\sin(\omega' t')$ where t' is as in Eq. 11 and drop the prime notation.

Before numerically analyzing the circadian version of Eqs. 12 and 13 driven by Eq. 32, we present some analytical approximations. Since both α, ε are assumed to be small, our analysis will depend on how the two relate to each other. If $\alpha \ll \varepsilon \ll 1$, the circadian rhythm defines the smallest perturbation and solutions to the model without the circadian rhythm presented in Section 2.1 (Eqs. 12 and 13 with $I(t) = I_0$) are valid zero-th order approximations to the circadian problem. If instead $\alpha = \mathcal{O}(\varepsilon)$ the analysis presented in Section 2.1 is no longer valid and the contribution of CRH hormonal storage and of the circadian rhythm must be jointly considered. We consider the two cases below.

3.1. Small circadian drive limit

We first consider the $\alpha \ll \varepsilon \ll 1$ case, and expand solutions to the circadian problem in Eqs. 12 and 13 in different orders of α as follows

$$x(t) = x_{\mathrm{u}}(t) + \alpha x_\alpha(t) + \mathcal{O}(\alpha^2), \tag{33}$$

$$y(t) = y_{\mathrm{u}}(t) + \alpha y_\alpha(t) + \mathcal{O}(\alpha^2), \tag{34}$$

where $(x_{\mathrm{u}}(t), y_{\mathrm{u}}(t))$ are solutions to the reduced non-circadian model, that solve Eqs. 12 and 13 with $I(t) = I_0$. These solutions equilibrate towards the steady-state values presented in Eqs. 17 and 18, $(x_{\mathrm{u}}(t \to \infty), y_{\mathrm{u}}(t \to \infty)) = (x_{\mathrm{u}}, y_{\mathrm{u}}) = (x_\pm, y_\pm)$, under the bistable conditions shown in Fig. 2. Upon inserting Eqs. 33 and 34 into the circadian model with $I(t)$ given by Eq. 32 we find

$$\frac{\mathrm{d}x_\alpha}{\mathrm{d}t} = -\varepsilon[x_\alpha + bo'(y_{\mathrm{u}})\mathrm{e}^{-bo(y_{\mathrm{u}})} y_\alpha], \tag{35}$$

$$\frac{\mathrm{d}y_\alpha}{\mathrm{d}t} = I_0 x_\alpha + \sin(\omega t) x_{\mathrm{u}} - (y_{\mathrm{u}} - y_1^*)(y_{\mathrm{u}} - y_2^*) y_\alpha. \tag{36}$$

To further simplify our analysis, without loss of generality we also assume that $(x_{\mathrm{u}}(t), y_{\mathrm{u}}(t))$ in Eqs. 35 and 36 are set as one of the two stable, fixed-points under $I(t) = I_0, (x_{\mathrm{u}}(t), y_{\mathrm{u}}(t)) = (x_{\mathrm{u}}, y_{\mathrm{u}}) = (x_\pm, y_\pm)$ so that Eqs. 35 and 36 become an inhomogeneous linear ODE system with respect to x_α, y_α. We can now rewrite Eqs. 35 and 36 as a matrix equation

$$\frac{\mathrm{d}\mathbf{x}_\alpha}{\mathrm{d}t} = \mathbf{A}\mathbf{x}_\alpha + \mathbf{b} \tag{37}$$

where $\mathbf{x}_\alpha(t) = (x_\alpha(t), y_\alpha(t))^T$, $\mathbf{b}(t) = (0, \sin(\omega t))^T x_{\mathrm{u}}$, and

$$\mathbf{A} \equiv \begin{bmatrix} -\varepsilon & -\varepsilon bo'(y_{\mathrm{u}})\mathrm{e}^{-bo(y_{\mathrm{u}})} \\ I_0 & -(y_{\mathrm{u}} - y_1^*)(y_{\mathrm{u}} - y_2^*) \end{bmatrix}. \tag{38}$$

Using standard methods to solve linear ODE systems driven by a periodic term we find

$$x_\alpha(t) = \frac{r_{11} r_{21} x_{\mathrm{u}}}{r_{11} r_{22} - r_{12} r_{21}} \left[\frac{\lambda_1 \sin(\omega t) + \omega\cos(\omega t)}{\omega^2 + \lambda_1^2} - \frac{\lambda_2 \sin(\omega t) + \omega\cos(\omega t)}{\omega^2 + \lambda_2^2}\right], \tag{39}$$

$$y_\alpha(t) = \frac{x_{\mathrm{u}}}{r_{11} r_{22} - r_{12} r_{21}} \left[\frac{r_{12} r_{21}(\lambda_1 \sin(\omega t) + \omega\cos(\omega t))}{\omega^2 + \lambda_1^2} - \frac{r_{11} r_{22}(\lambda_2 \sin(\omega t) + \omega\cos(\omega t))}{\omega^2 + \lambda_2^2}\right], \tag{40}$$

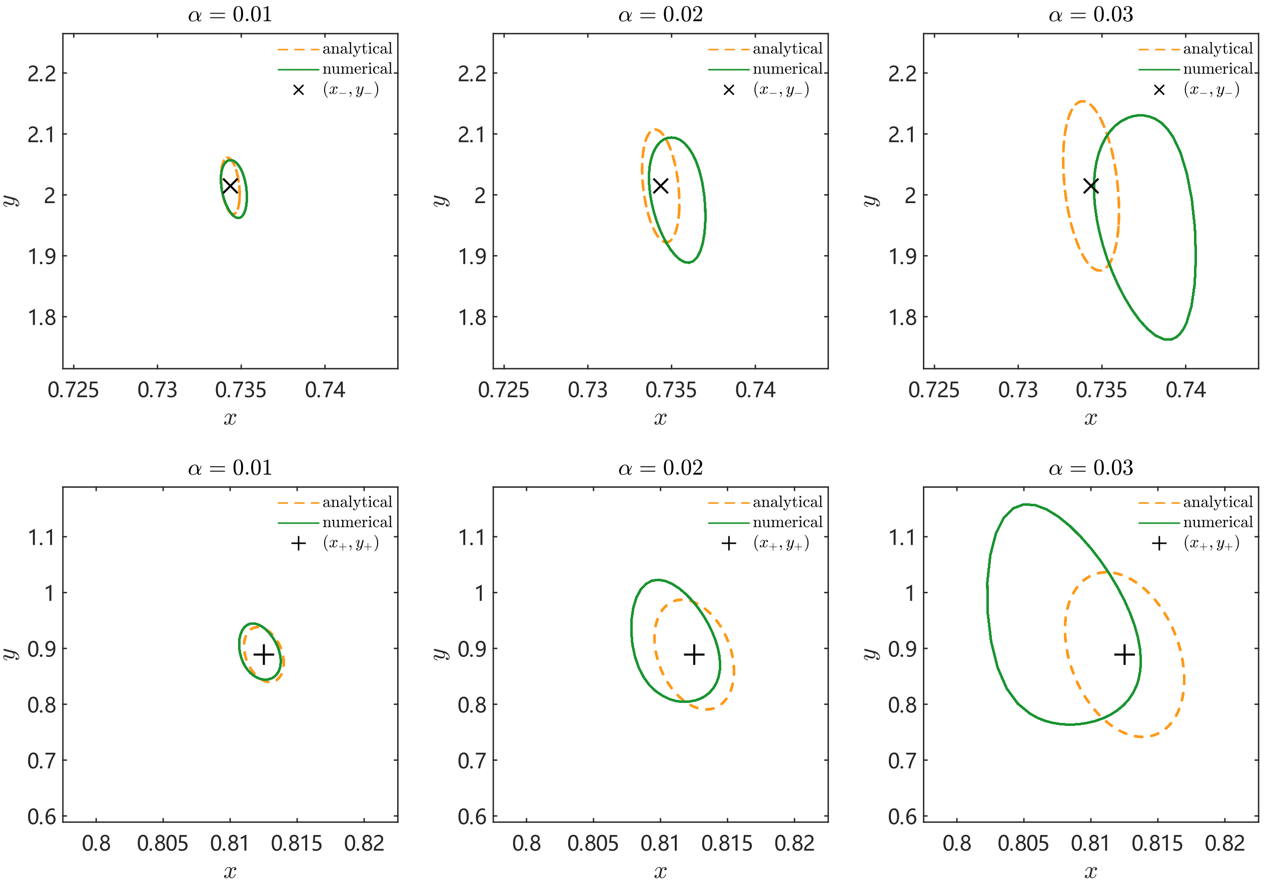

Fig. 5. Periodic orbits in (x, y) space driven by a circadian rhythm of amplitude $\alpha = 0.01, 0.02, 0.03$, from left to right. Analytical estimates are derived from Eqs. 33 and 34; numerical results are obtained from Eqs. 12 and 13. Parameters are listed in Sections 3.1, 3.2 and Table 1. For these values $\varepsilon = 0.0269$. Analytical estimates closely match numerical results for $\alpha \ll \varepsilon$, as detailed in the text. Top row: periodic orbits for perturbations around the fixed point $(x_{\mathrm{u}}, y_{\mathrm{u}}) = (x_-, y_-) = (0.73, 2.01)$. Bottom row: periodic orbits for perturbations around the fixed point $(x_{\mathrm{u}}, y_{\mathrm{u}}) = (x_+, y_+) = (0.81, 0.89)$.

where λ_1 and λ_2 are the eigenvalues of $\mathbf{A}$, corresponding to eigenvectors $\mathbf{r}_1 = (r_{11}, r_{12})^T$ and $\mathbf{r}_2 = (r_{21}, r_{22})^T$, respectively. We now compare and contrast the analytical results in Eqs. 33 and 34 truncated at first order in α and with (x_α, y_α) given in Eqs. 39 and 40 with numerical evaluation for the two $(x_\mathrm{u}, y_\mathrm{u})$ steady-states. For concreteness we specify $I_0 = 1, c_1^* = 15.5, c_2^* = 28$ and $k_1 = 2.4 \times 10^{-3}, k_2 = 8$ in addition to the other parameters given in Table 1. The above choices yield $y_1^* = 1.04, y_2^* = 1.87$ which fall in the bistability region shown in Fig. 2, and lead to $\varepsilon = 0.0269$. These choices ensure all constraints listed in Sect. 2 are met and that the reduced model is as close as possible to the original full model in Eqs. 1. Unless otherwise noted, the above parameters will be fixed at the above values for the remainder of this work.

In Fig. 5, we show numerical results for $\alpha = 0.01, 0.02, 0.03$. In the top row we consider perturbations around the fixed-point $(x_\mathrm{u}, y_\mathrm{u}) = (x_-, y_-)$. Similarly, those around the fixed point (x_+, y_+) are shown in the bottom row. For $\alpha = 0.01$, analytical results from Eqs. 33 and 34 agree well with numerical ones for both fixed-points, as α increases discrepancies between the two become more pronounced. This is to be expected, as the current analytical results are valid only insofar as $\alpha \ll \varepsilon = 0.0269$. Not shown in Fig. 5 are numerical and analytical results for values of $\alpha < 0.01$ which are also in good agreement. Note that the analytical approximations define curves that are centered about both fixed points $(x_\mathrm{u}, y_\mathrm{u})$. This is because the first-order approximations in Eqs. 39 and 40 contain superpositions of oscillatory terms with the same frequency ω, so that the dynamics in (x, y) space is symmetric about the central, fixed point.

3.2. Circadian drive comparable to stored CRH dynamics

We now assume $\alpha = \mathcal{O}(\varepsilon)$ and pose $\varepsilon = M\alpha$. Since the ε and α contributions in Eqs. 12 and 13 and in Eq. 32 are of the same order of magnitude, we must derive our analytical results independently of the results found in Section 2.1. We again expand with respect to α as follows

$$x(t) \;=\; x_\mathrm{u}(t) + \alpha x_\alpha^{(1)}(t) + \alpha^2 x_\alpha^{(2)}(t) + \mathcal{O}(\alpha^3), \tag{41}$$

$$y(t) \;=\; y_\mathrm{u}(t) + \alpha y_\alpha^{(1)}(t) + \alpha^2 y_\alpha^{(2)}(t) + \mathcal{O}(\alpha^3). \tag{42}$$

We expect the zero-th order solution, $(x_\mathrm{u}(t), y_\mathrm{u}(t))$ in Eqs. 41 and 42 to be the same as the fast solution to the non-circadian problem in Eqs. 21 and 22 given that now all perturbations arise to order α. We also include second order terms because, as we shall see below, the first order term $x_\alpha(t)$ is constant. Upon inserting Eqs. 41 and 42 into Eqs. 12 and 13, and using Eq. 32 we find the following sets of identities stemming from the three orders of α

$$\frac{\mathrm{d}x_\mathrm{u}}{\mathrm{d}t} \;=\; 0, \tag{43}$$

$$\frac{\mathrm{d}y_\mathrm{u}}{\mathrm{d}t} \;=\; I_0 x_\mathrm{u} - \left(\frac{1}{3}y_\mathrm{u}^3 - \frac{y_1^* + y_2^*}{2}y_\mathrm{u}^2 + y_1^* y_2^* y_\mathrm{u}\right), \tag{44}$$

$$\frac{\mathrm{d}x_\alpha^{(1)}}{\mathrm{d}t} \;=\; M(\bar{c}_\infty + \mathrm{e}^{-bo(y_\mathrm{u})} - x_\mathrm{u}), \tag{45}$$

$$\frac{\mathrm{d}y_\alpha^{(1)}}{\mathrm{d}t} \;=\; I_0 x_\alpha^{(1)} + \sin(\omega t) x_\mathrm{u}^{(1)} - (y_\mathrm{u} - y_1^*)(y_\mathrm{u} - y_2^*) y_\alpha^{(1)}, \tag{46}$$

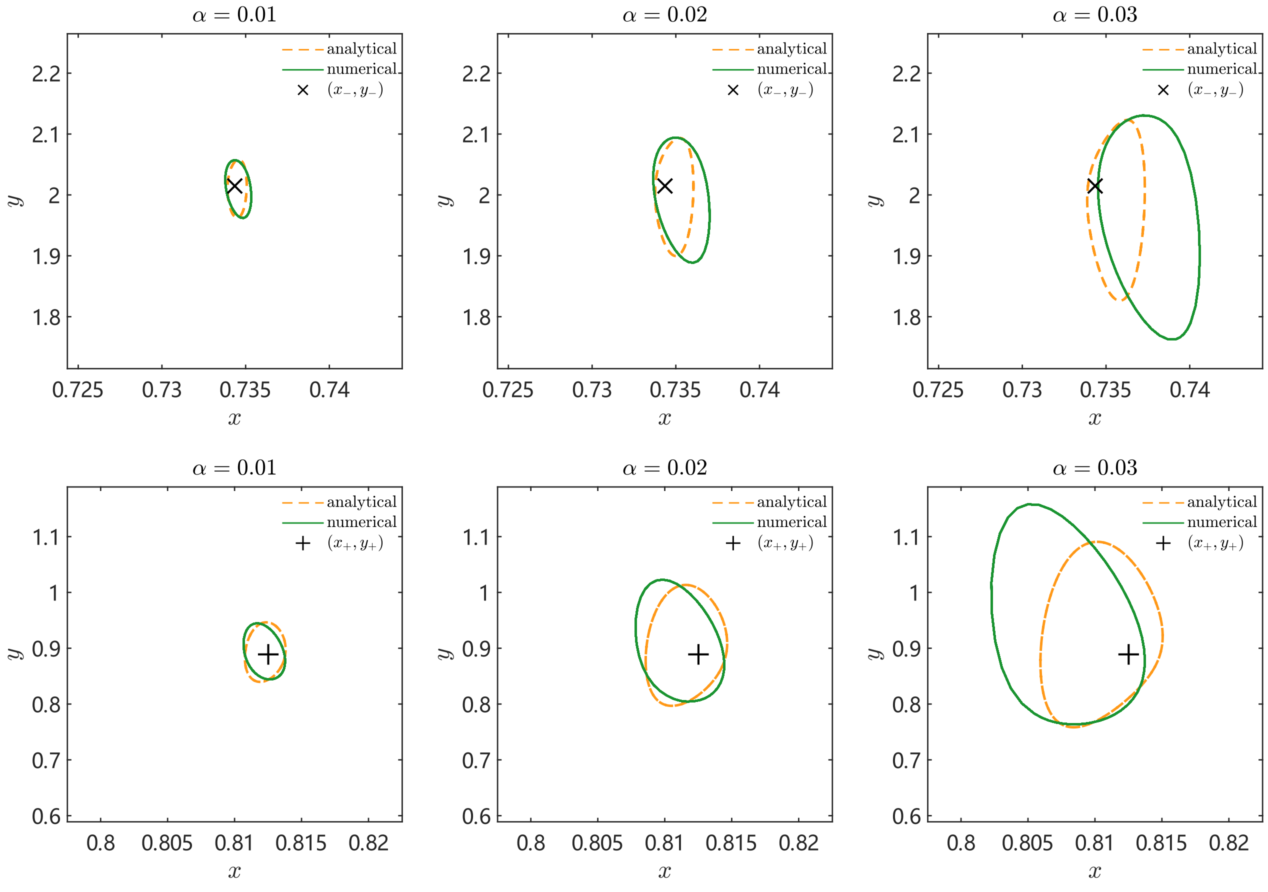

Fig. 6. Periodic orbits in (x, y) space driven by a circadian rhythm of amplitude $\alpha = 0.01, 0.02, 0.03$, from left to right. Analytical estimates are derived from Eqs. 41 and 42; numerical results are obtained from Eqs. 12 and 13. Parameters are listed in Sections 3.1, 3.2, Table 1 and Fig. 5. Analytical estimates closely match numerical results for $\alpha \sim \varepsilon$, as detailed in the text. Top row: periodic orbits for perturbations around $(x_\mathrm{u}, y_\mathrm{u}) = (x_-, y_-)$. Bottom row: periodic orbits for perturbations around $(x_\mathrm{u}, y_\mathrm{u}) = (x_+, y_+)$. Note the better agreement between analytic and numerical curves for $\alpha = 0.02, 0.03$ than Fig. .6.

$$\frac{\mathrm{d}x_\alpha^{(2)}}{\mathrm{d}t} = -M(bo'(y_\mathrm{u})\mathrm{e}^{-bo(y_\mathrm{u})}y_\alpha^{(1)} + x_\alpha^{(1)}), \tag{47}$$

$$\frac{\mathrm{d}y_\alpha^{(2)}}{\mathrm{d}t} = I_0 x_\alpha^{(2)} + \sin(\omega t)x_\alpha^{(1)} - \left(y_\mathrm{u}^2 y_\alpha^{(2)} + y_\mathrm{u}(y_\alpha^{(1)})^2 - \frac{y_1^* + y_2^*}{2}(2y_\mathrm{u}y_\alpha^{(2)} + (y_\alpha^{(1)})^2) + y_1^* y_2^* y_\alpha^{(2)}\right). \tag{48}$$

Solutions to Eqs. (43)–(48) will depend on the initial conditions. As expected, Eqs. 43 and 44 are the same as Eqs. 21 and 22, so the zeroth order dynamics is the same as in the non-circadian case. If we also assume that $(x_\mathrm{u}(t), y_\mathrm{u}(t)) = (x_\mathrm{u}, y_\mathrm{u}) = (x_\pm, y_\pm)$ are the time-independent equilibrium solutions to the non-circadian model, we also find that the right-hand side of Eq. 45 vanishes, leading to a constant value of $x_\alpha^{(1)}$. We can now solve Eq. 46 using the above assumptions. We find

$$y_\alpha^{(1)}(t) = y_\alpha(0)\mathrm{e}^{-\sigma t} + \frac{I_0 x_\alpha^{(1)}}{\sigma}(1 - \mathrm{e}^{-\sigma t}) + \frac{x_\mathrm{u}}{\omega^2 + \sigma^2}(\omega \mathrm{e}^{-\sigma t} + \sigma\sin(\omega t) - \omega\cos(\omega t)), \tag{49}$$

where

$$\sigma = (y_\mathrm{u} - y_1^*)(y_\mathrm{u} - y_2^*). \tag{50}$$

Note that $\sigma > 0$, since $y_\mathrm{u} = y_\pm$ and $y_+ < y_{1,2}^*$ and $y_- > y_{1,2}^*$. Eq. 49 depends on the constant value for x_α and on the initial condition $y_\alpha^{(1)}(0)$. If we assume $x_\alpha^{(1)}(0) = x_\alpha^{(1)} = y_\alpha^{(1)}(0) = 0$, the first order dynamics along the y axis is given by

$$y_\alpha^{(1)}(t) = \frac{x_\mathrm{u}}{\omega^2 + \sigma^2}(\omega \mathrm{e}^{-\sigma t} + \sigma\sin(\omega t) - \omega\cos(\omega t)). \tag{51}$$

We can also impose $x_\alpha^{(1)}(0) = x_\alpha^{(1)} \neq 0$ and assume $x_\alpha^{(1)}, y_\alpha^{(1)}(0)$ are related via

$$y_\alpha^{(1)}(0) = \frac{I_0 x_\alpha^{(1)}}{\sigma} - \frac{\omega x_\mathrm{u}}{\omega^2 + \sigma^2}, \tag{52}$$

to find a purely oscillatory solution

$$y_\alpha^{(1)}(t) = \frac{I_0 x_\alpha^{(1)}}{\sigma} + \frac{x_\mathrm{u}}{\omega^2 + \sigma^2}(\sigma\sin(\omega t) - \omega\cos(\omega t)). \tag{53}$$

To find the dynamics for $x_\alpha^{(2)}(t)$ and $y_\alpha^{(2)}(t)$ we assume $x_\alpha^{(1)}(0) = x_\alpha^{(1)} = 0$ for simplicity and set $y_\alpha^{(1)}(0)$ as in Eq. 52 leading to Eq. 53 so that

$$\frac{\mathrm{d}x_\alpha^{(2)}(t)}{\mathrm{d}t} = Mbo'(y_\mathrm{u})\mathrm{e}^{-bo(y_\mathrm{u})}\frac{x_\mathrm{u}}{\omega^2 + \sigma^2}(\omega\cos(\omega t) - \sigma\sin(\omega t)), \tag{54}$$

resulting in

$$x_\alpha^{(2)}(t) = Mbo'(y_\mathrm{u})\mathrm{e}^{-bo(y_\mathrm{u})}\frac{x_\mathrm{u}}{\omega(\omega^2 + \sigma^2)}(\omega\sin(\omega t) + \sigma\cos(\omega t) - \sigma) + x_\alpha^{(2)}(0). \tag{55}$$

The value of $x_\alpha^{(2)}(0)$ is arbitrary and can be set to zero; we can also choose $x_\alpha^{(2)}(0)$ so that the higher order solution $x_\alpha^{(3)}(t)$ remains oscillatory. This is shown in Appendix 7, where we also derive $y_\alpha^{(2)}(t)$, the solution to Eq. 48, which follows from tedious but straightforward computations.

In Fig. 6 we plot $(x(t), y(t))$ as derived from Eqs. 41 and 42, truncated to second order. For simplicity, we focus on purely periodic solutions, by setting the proper initial conditions to all the relevant orders of α. Specifically we use $x_\alpha^{(1)}(0) = x_\alpha^{(1)} = 0, y_\alpha^{(1)}(0)$ as given by Eq. 53 and $x_\alpha^{(2)}(0)$ and $y_\alpha^{(2)}(0)$ as given in Eqs. 88 and 86 respectively in Appendix 7. As done in Fig. 5, we consider both steady-state values $(x_\mathrm{u}, y_\mathrm{u}) = (x_\pm, y_\pm)$ and compare analytical and numerical evaluations for $\alpha = 0.01, 0.02, 0.03$, and $M = \varepsilon/\alpha$ with $\varepsilon = 0.0269$. The results shown in Fig. 6 reveal good agreement between analytical and numerical curves. Upon comparing Figs. 5 and 6 however we find that when $\alpha = 0.01 \lesssim \varepsilon$, Eqs. 33 and 34 are a closer approximation to the numerical results than Eqs. 41 and 42, but the reverse is true for $\alpha = 0.02, 0.03 \sim \varepsilon$, as can be expected since we are here considering the $\alpha = \mathcal{O}(\varepsilon)$ limit. The analytical approximations define curves that are not centered about the fixed points $(x_\mathrm{u}, y_\mathrm{u})$, to the contrary of what observed in Fig. 5. This is because the second-order approximations to Eqs. 47 and 48, shown in Eq. 55 and in Eq. 85 of Appendix 7, superimpose constants and oscillatory terms of frequency 2ω to the first order approximations centered about the fixed point and containing oscillations of frequency ω. These second-order terms break the symmetry about the fixed point, so that $(x_\mathrm{u}, y_\mathrm{u})$ is no longer central as $x(t)$ and $y(t)$ in Eqs. 41 and 42 oscillate. More details are shown in Appendix 8. We investigate the behavior of the system for larger values of α in Appendix 9. As can be seen, for $\alpha > 0.034$ period-doubling, subharmonics, and chaotic behavior emerge. While mathematically interesting, this limit does not allow to clearly distinguish between healthy and diseased states. In the remainder of this work we thus study stress-induced transitions to the HPA axis by keeping the amplitude of the circadian rhythm $\alpha < 0.034$.

4. Inducing transitions between steady states

We have hitherto assumed that the two stable states in the absence of the circadian drive, $(x_\mathrm{u}, y_\mathrm{u}) = (x_\pm, y_\pm)$ for $\alpha = 0$, represent a healthy and a diseased state. For concreteness and without loss of generality we identify (x_-, y_-) with the healthy state, and (x_+, y_+) with the diseased one, where $x_+ > x_-$ and $y_+ < y_-$. This choice is simply made for illustrative purposes, since as discussed in the Introduction, over- or under-expression of any of the hormones regulated by the HPA axis induce stress-related pathologies. As shown in Sect. 3 including the circadian drive yields limit cycles around both $(x_\pm, y_\pm)$ for $\alpha < 0.034$. Since at steady state limit cycles will orbit around them, we use these points as markers for healthy and/or diseased conditions even in the presence of the circadian drive. Finally, we limit our analysis to the $\alpha < 0.034$ regime, since larger values of α may lead to chaotic behavior.

We now study how the system transitions between the two limit cycles, or equilibrium values, in response to external perturbations. Within the diseased/healthy context introduced above, transitions from (x_-, y_-) to (x_+, y_+) (or from and to the limit cycles orbiting around them) represent the onset of disease, and the opposite progression, healing. These transitions may arise through parameter changes, which we associate to physical injury or surgical intervention, or in response to external input $I_\mathrm{ext}(t)$ such as psychological trauma, cognitive behavioral or exposure therapy. We only consider the latter scenario and study how an external input $I_\mathrm{ext}(t)$ superimposed to the circadian drive may or may not induce transitions between the two limit cycles. Thus, the basal value I_0 in Eq. 13 is replaced by $I_0 \to I_0 + \alpha\sin(\omega t) + I_\mathrm{ext}(t)$. While several shapes are possible we only consider illustrative examples where a simple pulse of fixed amplitude I_ext, duration T_ext, is applied at a given phase $\phi = \omega t$ (modulo 2π) of the circadian rhythm. The complete form of $I(t)$ includes basal, circadian, and reactive inputs to the HPA axis. In previous work, where the circadian drive was not included, the amplitude and duration of the external input were shown to greatly influence transitions between steady states [55,56]. Here, the acute stressors $I_\mathrm{ext}(t)$ may evoke strong responses, even surpassing the rhythmic ones; however the amplitude, duration and timing of the circadian drive contribute to the emergence of transitions in non-trivial ways.

4.1. Transitions between healthy and diseased states

In Figs. 7 to 11 we show trajectories under piece-wise constant perturbations of magnitude I_{ext} lasting for T_{ext} assuming the initial condition is along the normal or diseased limit cycles for $\alpha \neq 0$, or, if $\alpha = 0$, at the normal or diseased fixed point. Although T_{ext} in our computations is measured in non-dimensional units, according to the scaling provided in Eq. 11 and in Ref. [55], for concreteness, we describe following figures using dimensional values in the captions. Superimposing an external input to the circadian drive changes the shape of the fast y nullcline, but not of the slow x one. Following [55], we adopt the convention $I_{\text{ext}} \geqslant 0$, since the majority of neural circuits that project to the PVN are excitatory. This setting also avoids the emergence of negative values in the driving stimulus, since $I_0 + I_{\text{ext}} \geqslant \alpha$ when $I_0 = 1, \alpha < 0.034$. As a result, the fast y nullcline is compressed or stretched horizontally when the circadian and/or external drive are added to the basal I_0. If $I_{\text{ext}} > \alpha$, the smallest compression factor $I_0 + I_{\text{ext}} - \alpha$ arises when $\sin(\omega t) = -1$ and the largest compression factor $I_0 + I_{\text{ext}} + \alpha$ occurs when $\sin(\omega t) = 1$. If $I_{\text{ext}} < \alpha$ the nullcline is stretched by a factor $I_0 + I_{\text{ext}} - \alpha$ when $\sin(\omega t) = -1$ and similarly compressed by $I_0 + I_{\text{ext}} + \alpha$ when $\sin(\omega t) = 1$. The fast nullcline oscillates between the bounds provided by the two limits above. Whether transitions arise or not depends on the intricate interplay between the external input and the oscillating nullclines. In certain regimes transitions will arise, in others, they will not. Unless otherwise specified, parameters for the figures shown in this subsection and the next are as listed in Sect. 3.1, 3.2 and Table 1; illustration conventions are as described in Figs. 7 and 8.

We begin in Fig. 7 by showcasing the dynamics of the system when an external stressor $I_{\text{ext}} = 1$ is applied for $T_{\text{ext}} = 24$ hours with and without a circadian rhythm of varying amplitude α. The initial state is the healthy state at (x_-, y_-). The four panels show that increasing the magnitude of α affects the transitions from the healthy to the diseased state in a non-trivial way. As can be seen, in the absence of the circadian drive, I_{ext} induces a transition from (x_-, y_-) to (x_+, y_+), a modest amplitude $\alpha = 0.01$ hinders the

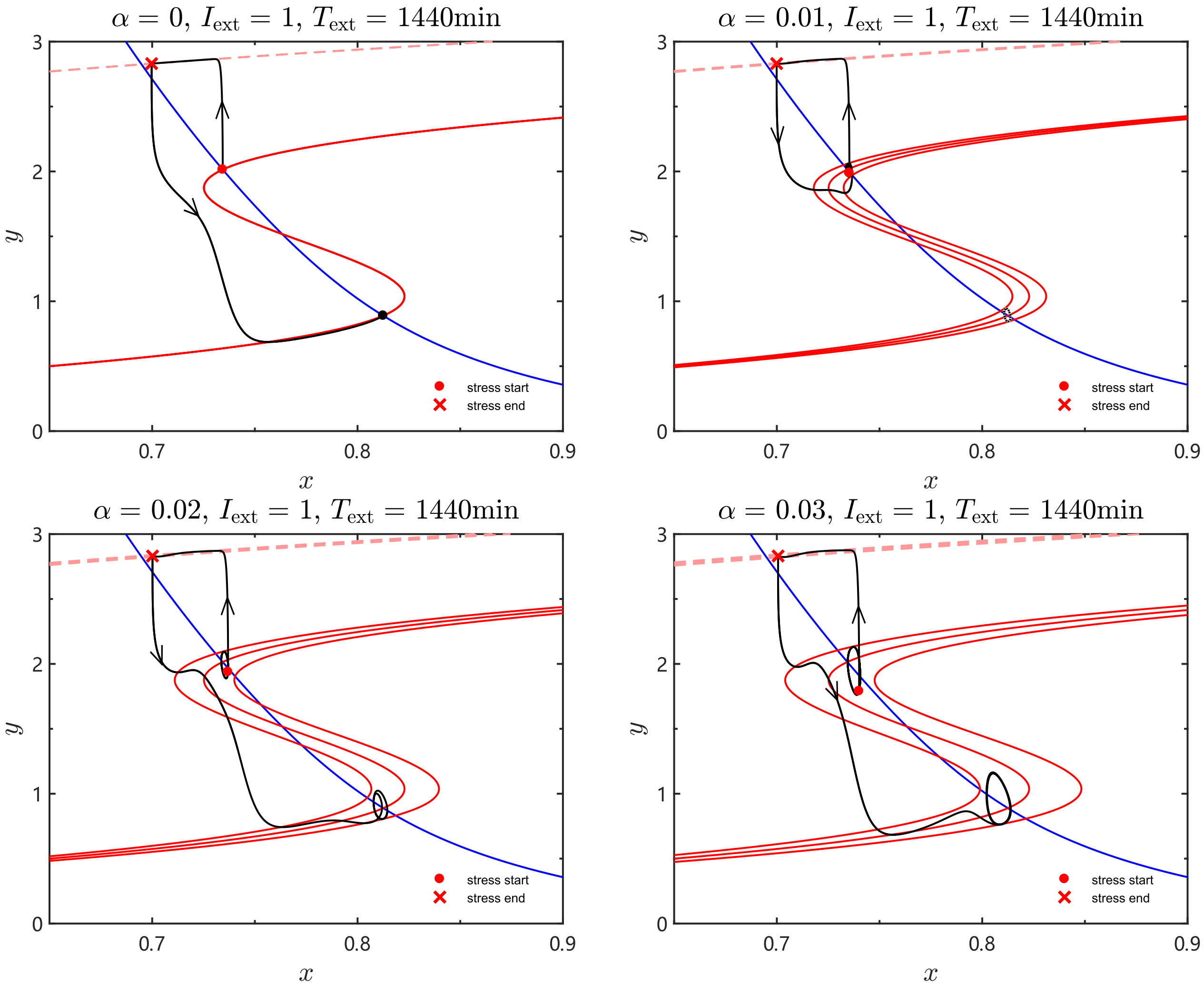

Fig. 7. Dynamics in phase space for (upper left) $\alpha = 0$, (upper right) $\alpha = 0.01$, (lower left) $\alpha = 0.02$, (lower right) $\alpha = 0.03$, when $I_{\text{ext}} = 1$ is active from $t = 0$ to $t = T_{\max} = 24$ hours and the system is initiated at the healthy (x_-, y_-) state. All other parameters are as listed in Sect. 3.1, 3.2, and Table 1. For $\alpha = 0$, the red solid curve is the fast nullcline when $I_{\text{ext}} = 0$, the red dashed curve is the fast nullcline when $I_{\text{ext}} = 1$, and the blue curve is the slow nullcline. The black curve is the trajectory. The three red solid curves that arise for $\alpha \neq 0$ are the fast nullclines when $I_{\text{ext}} = 0$ and the circadian drive defines a phase $\phi = -\pi/2, 0, \pi/2$ (modulo 2π) from right to left, respectively. The fast nullcline oscillates between these three curves. The red dashed curves are the fast nullclines when $I_{\text{ext}} = 1$. We also use three values of the circadian phase $\phi = -\pi/2, 0, \pi/2$, however the corresponding fast nullclines are not sufficiently resolved and appear as a single dashed line. The blue curve is the slow nullcline. When $\alpha = 0$, the external input I_{ext} is sufficient to induce a transition from the healthy state to the diseased one. Including a circadian drive with intermediate $\alpha = 0.01$ hinders the transition and the system remains in the healthy limit cycle. Further increases to $\alpha = 0.02, 0.03$ restores the transition to the diseased state.

transition and the system remains in the healthy state, but larger values $\alpha = 0.02, 0.03$ restore the transition to the diseased one. In the top row of Fig. 8 we initiate the system at the diseased state (x_+, y_+) and apply a pulse $I_{\text{ext}} = 0.02$ for $T_{\text{ext}} = 12$ hours with and without a circadian rhythm of amplitude $\alpha = 0.02$. For $\alpha = 0$ the system persists at the diseased state even after the pulse I_{ext} is applied, whereas for $\alpha = 0.02, I_{\text{ext}}$ induces a transition to the healthy state. In the bottom row of Fig. 7 the opposite outcome is observed. Here, the system is also originally initiated in the diseased state (x_+, y_+) and I_{ext} is applied for $T_{\text{ext}} = 12$ hours. In the absence of the circadian drive, the external input induces a transition to the healthy state, however a circadian rhythm with amplitude $\alpha = 0.03$ hinders the same transition, with I_{ext} unable to dislodge the system from the diseased state. These two examples show that the circadian drive may strongly influence how external pulses, representing therapeutic intervention, affect the system. Subjects may thus respond differently to cognitive behavior treatment depending on how sensitive they are to the circadian rhythm.

To understand the role of the magnitude I_{ext}, in Fig. 9 we consider the non-circadian $\alpha = 0$ case, where the external pulse I_{ext} is active from $t = 0$ to $t = T_{\max} = 48$ hours and where the magnitude is increased from $I_{\text{ext}} = 0.5$ to $I_{\text{ext}} = 0.8$, while keeping all other parameters fixed. In both cases, the external perturbation dislodges the system from the diseased state (x_+, y_+) towards the perturbed equilibrium given by the intersection of the slow nullcline with the perturbed fast nullcline. Since T_{ext} is large enough, the system will settle in this new equilibrium, marked by the red cross in Fig. 9. However, once I_{ext} is terminated, the system must return to either of the original steady states. For $I_{\text{ext}} = 0.5$, the perturbed equilibrium falls into the basin of attraction of the original healthy equilibrium, so the trajectory will settle into the healthy steady state and a transition is recorded, as shown in the left panel of Fig. 9. The value $I_{\text{ext}} = 0.8$ instead leads the system further away from the original nullclines so that here the new perturbed equilibrium, marked by the red cross, falls into the basin of attraction of the original diseased state. As a result, after a large excursion in

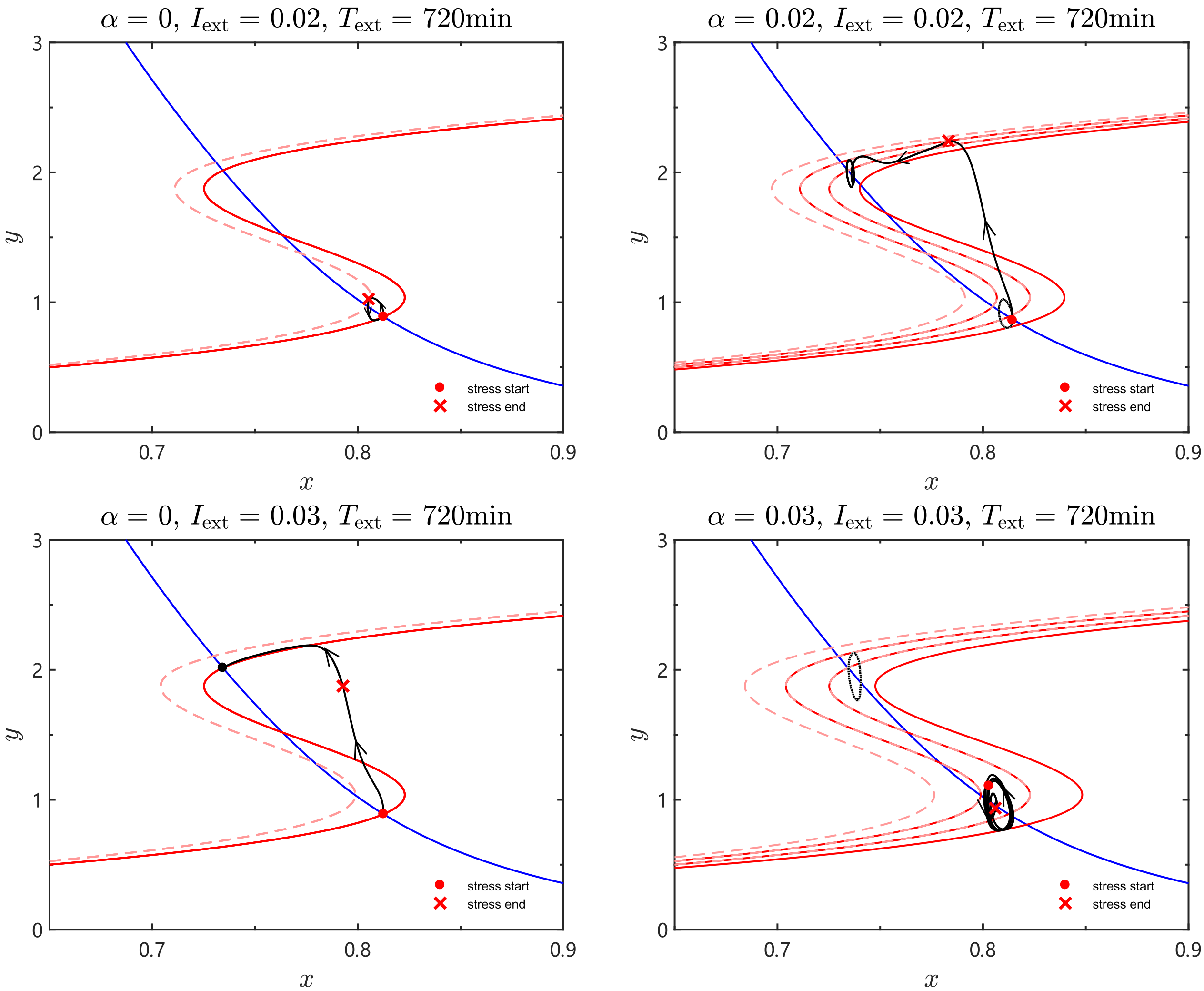

Fig. 8. Dynamics in phase-space for (upper left) $\alpha = 0$ and (upper right) $\alpha = 0.02$ when $I_{\text{ext}} = 0.02$ is active from $t = 0$ to $t = T_{\text{ext}} = 12$ h, and for (lower left) $\alpha = 0$ and (lower right) $\alpha = 0.03$ when $I_{\text{ext}} = 0.03$ is active for $T_{\text{ext}} = 12$ hours, from $t = 720$ min ($\phi = \pi$) to $t = 1440$ min. The initial condition is always the diseased (x_+, y_+) state. The first row shows the circadian-induced, diseased-to-healthy transition. The second row shows the circadian drive impeding the same transition. In the left panels, the solid red curves are the fast nullcline in the basal state, $I_{\text{ext}} = \alpha = 0$. The dashed red curves are the fast nullcline when $I_{\text{ext}} \neq 0$ and $\alpha = 0$. The blue curve is the slow nullcline. In the right panels, the three red solid curves to the outermost right are the fast nullcline when $I_{\text{ext}} = 0$ and the circadian drive defines a phase $\phi = -\pi/2, 0, \pi/2$, from right to left, respectively. For $I_{\text{ext}} = 0, \alpha \neq 0$, the fast nullcline oscillates between them. The three dashed curves to the outermost left are the fast nullcline when $I_{\text{ext}} \neq 0$ and similarly $\phi = -\pi/2, 0, \pi/2$ from right to left. For $I_{\text{ext}} \neq 0$ the fast nullcline oscillates between them. Due to the numerical values of I_{ext}, α some of the fast nullclines superimpose. From right to left, the driving terms of the fast nullclines are $I_0 - \alpha, I_0 = I_0 + I_{\text{ext}} - \alpha$ (superimposed), $I_0 + \alpha = I_0 + I_{\text{ext}}$ (superimposed), $I_0 + I_{\text{ext}} + \alpha$. We plot the healthy limit cycle as a dotted black curve in the lower right panel for reference.

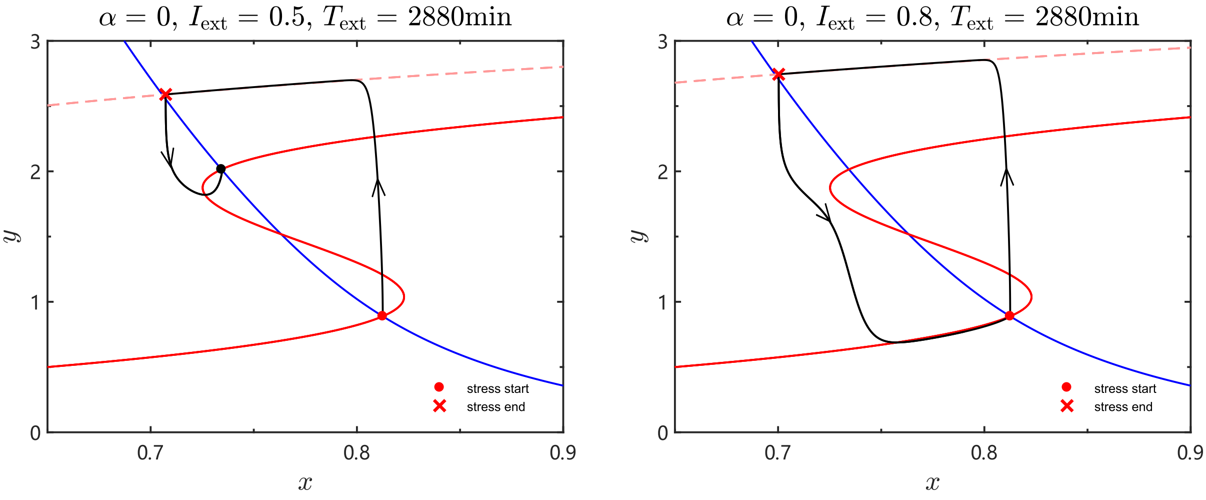

Fig. 9. Dynamics in phase-space for (left) $I_{\rm ext} = 0.5$ and (right) $I_{\rm ext} = 0.8$ active from $t = 0$ to $t = T_{\rm ext} = 48$ hours. In the left panel, $I_{\rm ext} = 0.5$ causes a transition from the initial diseased state to the perturbed equilibrium, which falls into the basin of attraction of the non-perturbed healthy equilibrium. Once $I_{\rm ext}$ is terminated, the system transitions to this healthy state. A larger $I_{\rm ext} = 0.8$ disrupts the dynamics further and the new perturbed equilibrium falls into the basin of attraction of the non-perturbed diseased state. After a long excursion, the termination of $I_{\rm ext}$ returns the system to the diseased state.

phase space, the trajectory returns towards the diseased state. This is a slightly counter-intuitive finding, since one may expect that larger pulses $I_{\rm ext}$ may better facilitate transitions to the healthy state.

In Fig. 10 we show that another determinant of the transition between states is given by the starting time of $I_{\rm ext}$ relative to the phase of the circadian rhythm. In the left panel we apply two external inputs $I_{\rm ext} = 0.2$ lasting $T_{\rm ext} = 24$ hours. In the first case $I_{\rm ext}$ is applied from $t = 0$ to $t = T_{\rm ext} = 1440$ min. The trajectory in the black solid line, is perturbed but stays in the healthy state. In the second case, although similarly $I_{\rm ext} = 1$ and $T_{\rm ext} = 24$ hours, the external input is delayed, starting at $t = 480$ min and terminating at $t = 1920$ min. As can be seen, the transition to the diseased state does occur. The same dynamics is observed in the right panel where the system is initiated at the diseased state and two external inputs $I_{\rm ext} = 1$ lasting $T_{\rm ext} = 27$ hours are applied. When $I_{\rm ext}$ is applied from $t = 0$ to $t = T_{\rm ext} = 1620$ min, a transition towards the healthy state arises, whereas when the external stressor is delayed and initiated at $t = 720$ min and terminated at $t = 2340$ min, the transition does not occur and the trajectory returns to the diseased state.

The effects of duration of the external input $I_{\rm ext}$ are shown in Fig. 11 where $I_{\rm ext}$ is applied at $t = 0$ but for different durations $T_{\rm ext}$. In the left panel, the system starts in the healthy state and $\alpha = 0.02$. When an external stressor $I_{\rm ext} = 0.3$ is applied for $T_{\rm ext} = 12$ hours (solid black curve), a transition to the diseased state is observed, however when $I_{\rm ext} = 0.3$ is applied for $T_{\rm ext} = 18$ hours (dash-dot black curve), the system remains at the healthy state. Similarly, in the right panel the system starts in the diseased state and $\alpha = 0.01$. When an external pulse $I_{\rm ext} = 1$ is applied for $T_{\rm ext} = 36$ hours (solid black curve), the system does not transition to the healthy state, however when $I_{\rm ext} = 1$ is applied for $T_{\rm ext} = 39$ hours (dash-dot black curve), a transition to the healthy state is observed. Upon further increasing $T_{\rm ext}$ to $T_{\rm ext} = 48$ hours, the sys-

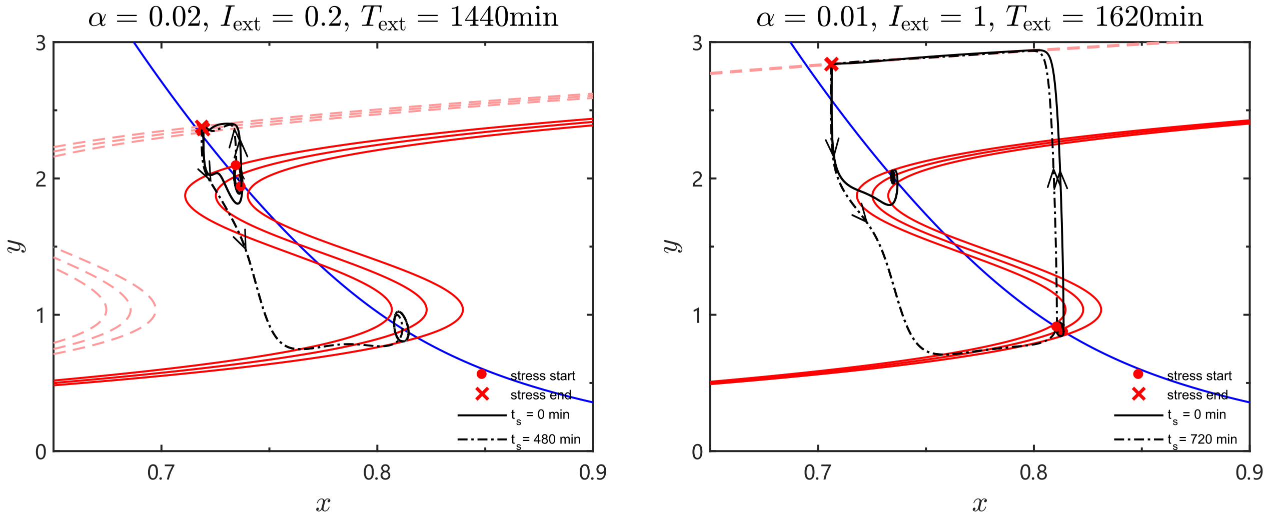

Fig. 10. Dynamics in phase-space where an external input of magnitude $I_{\rm ext}$ lasting $T_{\rm ext}$ is applied at different phases ϕ relative to the circadian rhythm. In the left panel $I_{\rm ext} = 0.2$ is applied for a system initially at the healthy state, for $T_{\rm ext} = 1440$ min, with start times of $t = 0$ ($\phi = 0$, solid black curve) and $t = 480$ min ($\phi = 2\pi/3$, dash-dot black curve). The amplitude of the circadian rhythm is set at $\alpha = 0.02$. When $I_{\rm ext}$ is initiated at $t = 0$ the trajectory remains at the healthy state, when $I_{\rm ext}$ is initiated at $t = 480$ min the trajectory transitions to the diseased state. Similar dynamics are shown in the right panel when $I_{\rm ext} = 1$ is applied for a system initially at the diseased state, for $T_{\rm ext} = 1620$ min, with start times of $t = 0$ ($\phi = 0$, solid black curve) and $t = 720$ min ($\phi = \pi$, dash-dot black curve). When $I_{\rm ext}$ is initiated at $t = 0$ the trajectory transitions to the healthy state, when $I_{\rm ext}$ is initiated at $t = 720$ min the trajectory returns to the diseased state.

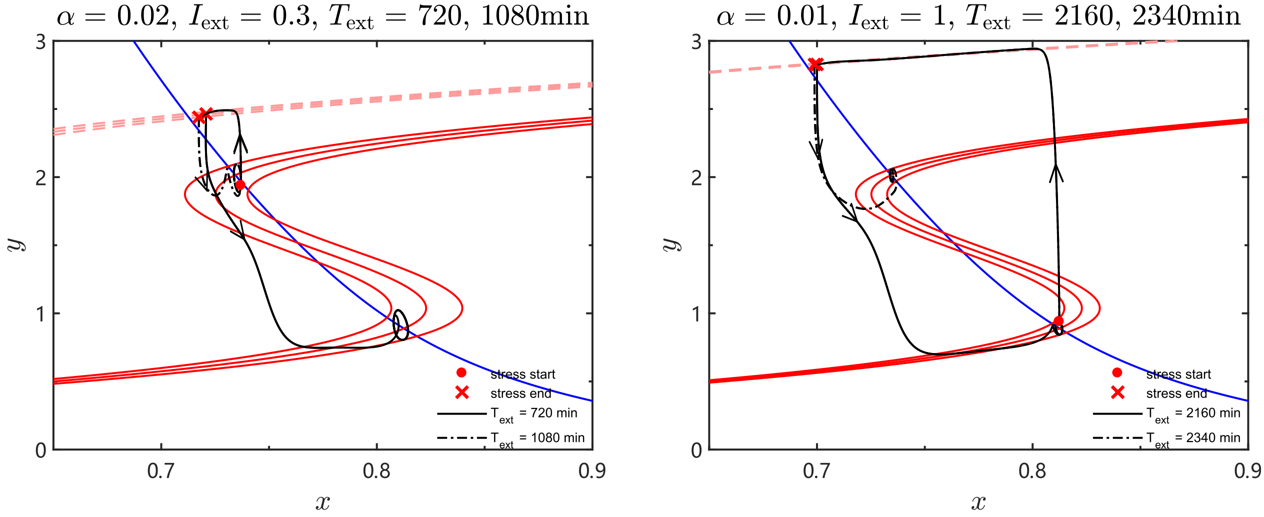

Fig. 11. Dynamics in phase-space when an external input $I_{\rm ext}$ lasting for variable $T_{\rm ext}$ is applied in the presence of the circadian rhythm. In the left panel $I_{\rm ext} = 0.3$ is applied to the healthy state at time $t = 0$ ($\phi = 0$) for $T_{\rm ext} = 720$ min (solid black curve), and for $T_{\rm ext} = 1080$ min (dash-dot black curve). The amplitude of the circadian rhythm is set at $\alpha = 0.02$. When $T_{\rm ext} = 720$ min the external stressor induces a transition to the diseased state, when $T_{\rm ext} = 1080$ min no transition arises. Similarly in the right panel $I_{\rm ext} = 1$ is applied for a system initially at the diseased state, at time $t = 360$ min ($\phi = \pi/2$) for $T_{\rm ext} = 2160$ min (solid black curve) and $t = 2340$ min (dash-dot black curve) for $\alpha = 0.01$. In the first case the trajectory returns to the diseased state, in the second case, the pulse allows the system to transition to the healthy state.

tem will remain in the diseased state. We do not plot this case, but the trajectory follows very closely the one observed for $T_{\rm ext} = 36$ hours. These results show that the amplitude of the circadian drive α, the magnitude $I_{\rm ext}$, onset phase ϕ, and duration of the external input $T_{\rm ext}$ affect transitions between states in subtle ways. Finally, Figs. 9–11 show that under stressed conditions, trajectories may access perturbed equilibria that persist as long as the stress remains active. These perturbed equilibria can be considered meta-stable states that vanish once the external stressor/input is removed. The system will then return to its original healthy or diseased, non-stressed state or transition to the opposite one.

4.2. Transition diagrams between healthy and diseased states

In this section we study the interplay between $I_{\rm ext}, T_{\rm ext}, \alpha$ and ϕ, by plotting transition diagrams in $\{T_{\rm ext}, I_{\rm ext}\}$ space for two possible initial conditions (healthy and diseased) and several values of α, ϕ. These diagrams will indicate whether a transition has occurred or not after a stressor or pulse characterized by $\{T_{\rm ext}, I_{\rm ext}\}$ applied at phase ϕ is terminated.

In Fig. 12 we start the system in the healthy (left panel) and the diseased (right panel) states and show the final equilibrium configuration in the absence of the circadian rhythm ($\alpha = 0$). As can be seen in the left panel, transitions from the healthy (x_-, y_-) to the diseased state (x_+, y_+) arise for sufficiently large external stressors $I_{\rm ext}$ of sufficient duration $T_{\rm ext}$. Interestingly, in the right-hand panel, long lived pulses are associated with transitions from the diseased (x_+, y_+) to the healthy state (x_-, y_-) only if $I_{\rm ext}$ is of intermediate value, but not too small or too large. Why would large pulses that last long enough not induce transitions? The answer is the asymmetry induced by selecting $I_{\rm ext} > 0$. This choice always compresses the fast nullcline and its corresponding limit cycle to the left. When starting in the diseased state, small values of $I_{\rm ext}$ are not large enough to sufficiently perturb the system, so no transitions are

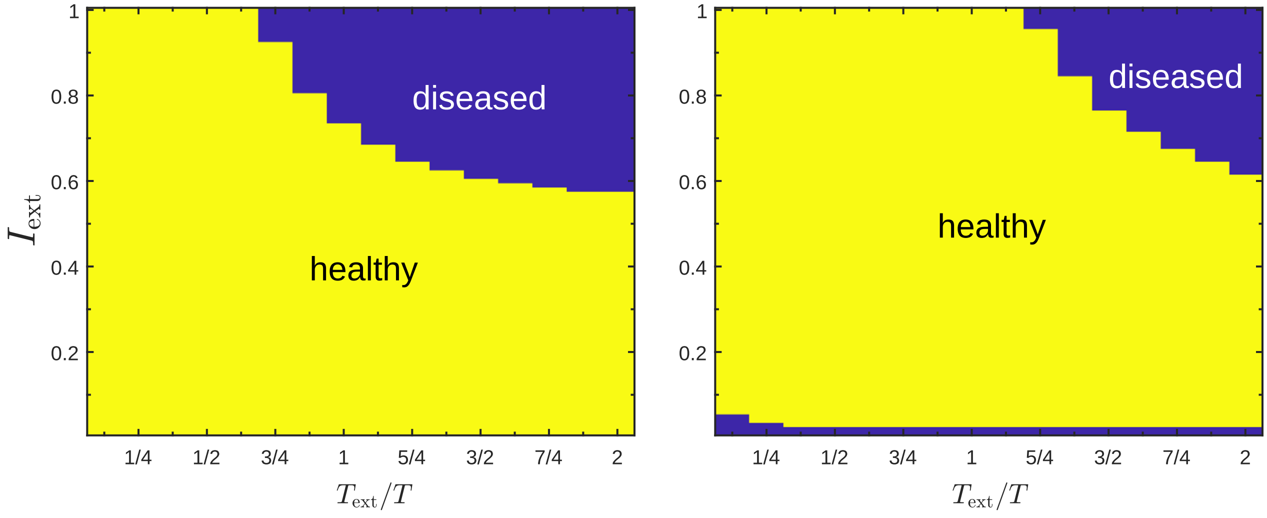

Fig. 12. Final equilibrium states in $\{T_{\rm ext}, I_{\rm ext}\}$ space in the absence of the circadian rhythm ($\alpha = 0$), starting from the healthy (left) and diseased state (right). Durations are set as $T_{\rm ext} = m_T T/8$, with $1 \leqslant m_T \leqslant 16$, magnitudes are set at $I_{\rm ext} = 0.01\,m$, with $1 \leqslant m \leqslant 100$, defining 1600 combinations, corresponding to 1600 rectangles centered at $(T_{\rm ext}, I_{\rm ext})$. Colors represent the final equilibrium state after cessation of the $(T_{\rm ext}, I_{\rm ext})$ perturbation: yellow ones indicate a final healthy equilibrium at (x_-, y_-), purple ones indicate a final diseased equilibrium at (x_+, y_+). Note that large and long perturbations always lead to the diseased state, regardless of the initial configuration.

observed, as can be expected. Intermediate I_{ext} values may induce transitions, however if I_{ext} is too large, the compression to the left may cause the intersection between the fast and slow nullclines corresponding to the diseased (x_+, y_+) state to vanish. The trajectory must leave the initial (diseased) equilibrium and start evolving towards the perturbed one arising under I_{ext}. For short durations T_{ext}, upon termination of the external pulse, the system may still be en route to the perturbed equilibrium and/or be in the basin of attraction of the non-perturbed healthy state and a transition will be observed. However, when T_{ext} is sufficiently large, the trajectory will be in the proximity, or at, the perturbed equilibrium while I_{ext} is still active. Once the pulse is terminated, if I_{ext} is large enough, the perturbed equilibrium may be sufficiently distant from the non-perturbed nullclines and fall into the basin of attraction of the original, diseased equilibrium. In this case, there will be a large excursion in (x, y) space but the system will eventually return to the original diseased state. Representative dynamics are shown in Fig. 9 where an intermediate value of I_{ext} for sufficiently large T_{ext} induces a transition, but larger values of I_{ext} do not. These results show that large, long lived external inputs will always result in the system stabilizing at the diseased state, regardless of initial conditions, indicating that therapeutic intervention should be applied judiciously.

We present similar results in Figs. 13 to 18 where the amplitude of the circadian rhythm is set at $\alpha = 0.01, 0.02, 0.03$, and where the system is initiated at the healthy state in Figs. 13–15, and at the diseased state in Figs. 16–18. Plotting conventions are the same as in Fig. 12; however, here we also consider the phase at which I_{ext} is superimposed on the initial, healthy or diseased, limit cycle relative to the circadian rhythm. Specifically, we set $\phi = n_\phi \pi/4$, with $0 \leqslant n_\phi \leqslant 7$, resulting in eight panels for each choice of $\alpha \neq 0$. see Fig. 17.

In Fig. 13, I_{ext} is applied when $\alpha = 0.01$ and the system is in a limit cycle about the healthy state. For relatively low T_{ext} and/or I_{ext}, no transitions to the diseased state occur and the system remains in the healthy state. However, external stressors with longer duration and larger magnitude do not necessarily imply a higher likelihood of transitioning to the diseased state, as observed in the non-circadian case. Rather, regions in $\{T_{\mathrm{ext}}, I_{\mathrm{ext}}\}$ space where transitions to the diseased state occur are separated from those where no transitions occur by an undulating parameter boundary exhibiting multiple minima in I_{ext}, a consequence of the pulsatile circadian rhythm imposed on the HPA dynamics. For a null onset phase of the external stressor relative to the circadian rhythm, $\phi = n_\phi = 0$, the nadir of the separatrix emerges at $T_{\mathrm{ext}} = 3/2T$. As ϕ increases from $\phi = 0$ to $\phi = 7\pi/4$, this minimum shifts to shorter T_{ext} following an approximate $T_{\mathrm{ext}} = (12 - n_\phi)T/8$ trend. At $\phi = \pi$, an additional nadir emerges at $T_{\mathrm{ext}} = 2T$, which follows a $T_{\mathrm{ext}} = (20 - n_\phi)T/8$ trend as ϕ further increases. The time at which the stressor ends defines a phase relative to the circadian rhythm given by $\phi_{\mathrm{end}} = \phi + 2\pi T_{\mathrm{ext}}/T$ where we add the onset phase ϕ and the phase defined by the duration of the external stressor $2\pi T_{\mathrm{ext}}/T$. For all recorded minima in Fig. 13, $\phi_{\mathrm{end}} = \pi$ (modulo 2π), indicating that the lowest I_{ext} that can be applied to induce a transition from the healthy to the diseased limit cycle should last long enough, and be terminated when the circadian rhythm is at $\alpha \sin(\omega t) = \alpha \sin(\phi_{\mathrm{end}}) = 0$.

Qualitatively, low values of T_{ext} and/or I_{ext} do not allow the system, initially at the healthy limit cycle, to reach the diseased one, so transitions are unlikely. Once T_{ext} and/or I_{ext} are sufficiently large however, the trajectory will reach the perturbed limit cycle and remain anchored to it. Further increasing T_{ext} and/or I_{ext} will still result in the trajectory oscillating about the perturbed healthy limit cycle so that beyond a certain threshold the magnitude of T_{ext} and/or I_{ext} become irrelevant. Thus, upon terminating the external input, whether the trajectory returns to the healthy limit cycle or is able to escape towards, and finally attracted into, the diseased one, is highly sensitive to the end phase ϕ_{end}, which determines the position of the oscillating fast nullcline, and much less to T_{ext} and/or I_{ext}. The optimal end phase for the trajectory to remain at the diseased state is the "neutral" configuration $\phi_{\mathrm{end}} = \pi$.

These features persist for $\alpha = 0.02$, as shown in Fig. 14 where all minima in $\{T_{\mathrm{ext}}, I_{\mathrm{ext}}\}$ space are marked by an end phase $\phi_{\mathrm{end}} = \pi$ (modulo 2π), just as for $\alpha = 0.01$. The region where the transition is observed (depicted in purple) however is larger than for $\alpha = 0.01$. Here, the larger oscillations induced by the circadian drive allow lower values of T_{ext} and/or I_{ext} to induce transitions. Finally, in Fig. 15 where $\alpha = 0.03$ and circadian oscillations are even wider, transitions occur in most of phase space, except for very low values of I_{ext}.

In Figs. 16–18 we initiate the system at the diseased limit cycle around (x_+, y_+) and set the amplitude of the circadian rhythm to $\alpha = 0.01, 0.02, 0.03$, respectively. In Fig. 16 a small parameter region with low I_{ext} and a broad range of T_{ext} is observed where trajectories remain at the diseased state. For slightly larger values of

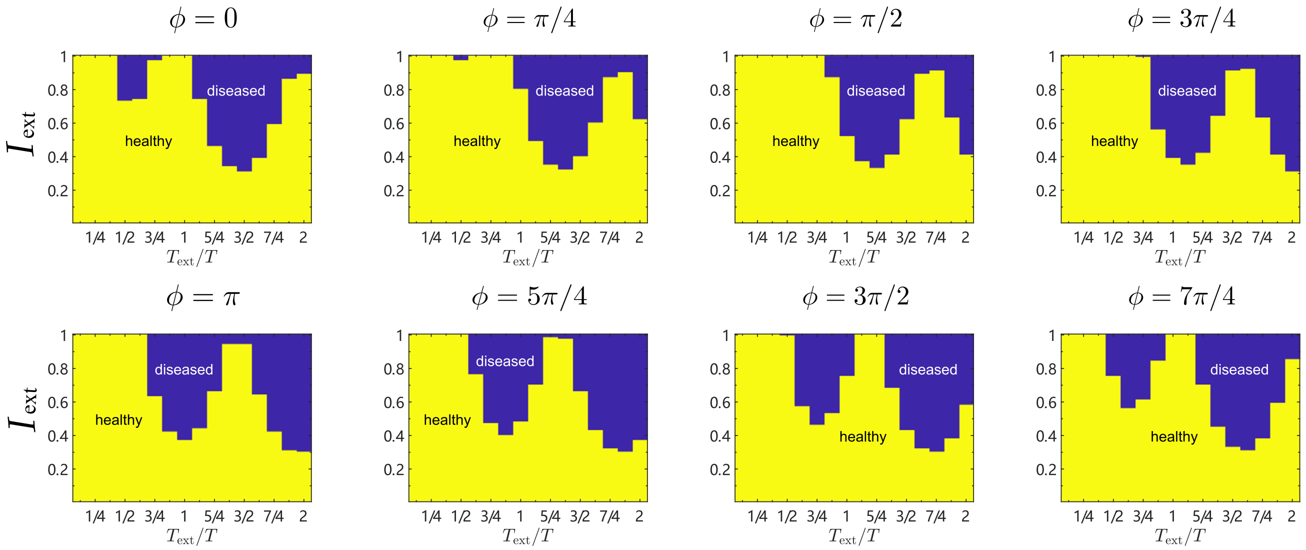

Fig. 13. Starting from a healthy-state limit cycle, we show the final configurations in $\{T_{\mathrm{ext}}, I_{\mathrm{ext}}\}$ space for $\alpha = 0.01$ and eight values of the start time of the external stress relative to the circadian drive ϕ.

I_{ext}, pulses with intermediate durations T_{ext} will induce a transition to the healthy limit cycle; however, larger T_{ext} may not be conducive to transitions. The dynamics here mirrors the non-circadian $\alpha = 0$ case, where large values of I_{ext} may cause the diseased steady state to vanish. Finally note that the boundaries between regions in $\{T_{\mathrm{ext}}, I_{\mathrm{ext}}\}$ space where transitions do and do not emerge shares some similarities to the ones observed in Figs. 13 to 15.

5. Discussion and conclusions

Building on previous work, we incorporated a circadian cycle into a dynamical systems model of the HPA axis. We start by considering the dynamics and interplay of five main quantities involved in the HPA axis response to external perturbations (stored CRH, circulating CRH, ACTH, cortisol and glucocorticoid receptor concentrations), and introduce several simplifications to build a simpler two-dimensional reduced model. We first review the non-circadian limit and neglect the known delay in ACTH activation of adrenal gland secretion of cortisol. This delay of approximately fifteen minutes allows for the emergence of ultradian (hourly) oscillations. Since we are interested in the effects of the circadian (diurnal) cycle, which unfolds over a longer time frame than hourly oscillations, we do not include delays, and refer the interested reader to previous work where its impacts are discussed [55,56]. We also note that the dynamics of ACTH, cortisol and glucocorticoid receptor concentrations, evolve on much shorter time scales than stored CRH, allowing us to consider the steady state values of these quantities, effectively projecting the original system of five equations to a set of two coupled ones for stored and circulating CRH. Of these, the first evolves on a longer time scale, of the order of hours, the other on a shorter one on the order of minutes. Once the equations for stored and circulating CRH are solved, values for the other quantities (ACTH, cortisol and glucocorticoid receptors) can be derived by substitution in the respective steady state expressions. Using order of magnitude estimates for the various terms involved we finally express the right-hand side of the dynamics of circulating CRH via a cubic expression. This form bears no physiological relationship to the actual evolution of circulating CRH, however it is a very good ad hoc substitute in that it allows for a thorough mathematical analysis while preserving the main features of the system, namely the emergence of bistability, *i.e.* of two steady states, one marked by low values of circulating CRH, and the other by higher values. These stable states emerge as intersections of a fast nullcline, when circulating CRH reaches equilibrium, and a slow nullcline, when stored CRH reaches equilibrium. We interpret them as diseased and healthy states, respectively. After analyzing the two coupled, self-contained equations using a cubic approximation (without the circadian rhythm, Eqs. 12 and 13), we included the circadian drive and considered several possibilities for the amplitude of the circadian component relative to the evolution of the slow nullcline. We show that low amplitudes of the circadian rhythm turn the two fixed points from the non-circadian system into limit cycles about them, allowing us to identify healthy and diseased limit cycles. We also obtain analytical approximations for them. For larger values of the circadian amplitude, the two limit cycles merge into one and chaotic behavior is observed, reminiscent of Duffing oscillator dynamics. Finally, we include an external, constant pulse input (box function) of amplitude I_{ext} and duration T_{ext}, and investigate the trajectories of the system and whether transitions from healthy to diseased states or vice versa can occur. We find that whether transitions arise or not depends in a complex way on $I_{\mathrm{ext}}, T_{\mathrm{ext}}, \alpha$ and the phase ϕ at which the external input is applied or terminated relative to the circadian rhythm. Interestingly, we find that an important determinant for the existence of transitions depends on the phase ϕ_{end} at which the external stressor is terminated relative to the circadian rhythm. We also find that large perturbations I_{ext} applied for sufficiently long times T_{ext} on the diseased state may greatly disrupt the system leading to large excursions in the dynamics of stored and circulating CRH. This disruption may however be temporary and the system will eventually return to the original diseased state. In the context of therapeutic intervention, this result may signify that large, long lasting external inputs may not be as effective as more moderate ones, applied for shorter times. We also find that due to the nullcline structure of the system, remaining in/transitioning to the diseased state is more likely for large circadian amplitudes α than for smaller ones.

In this work we have assumed that the diseased state corresponds to larger stored CRH and lower circulating CRH, exemplified by the steady state (or the limit cycle) about (x_+, y_+). This configuration corresponds to low circulating levels of cortisol since $x = c_{\mathrm{s}}$ and, at steady state, $c_{\mathrm{s}} = \bar{c}_\infty + \mathrm{e}^{-bo}$ is a decreasing function of cortisol. Conversely, the healthy equilibrium or limit cycle at (x_-, y_-) is characterized by lower stored CRH (and higher cortisol) and larger circulating CRH. This is one of many choices, since other pathologies may exhibit different relative hormonal levels between healthy and diseased states. For example, acute manifestations of major depressive disorder (MDD) are marked by high levels of secreted CRH and of cortisol [17,21], implying that the healthy state can be identified with (x_+, y_+) and the diseased one with (x_-, y_-). In this case the external stressor I_{ext} applied to the healthy state can be identified as a triggering event that leads to MDD, or, if applied to the diseased state, as a pulse associated to exposure or cognitive behavioral therapy (CBT). *Mutatis mutandis*, our results would also indicate that transitions to MDD may be more easily induced by lower values of the circadian amplitude α, consistent with experimental findings that find blunted amplitude of the circadian rhythm in depressed patients [67]. On the other hand, PTSD is often associated with low levels of cortisol but relatively high values of CRH. This would translate to large (c_{s}, c) values for the diseased state, or equivalently large (x, y). In our specific model, the slow nullcline carries a negative slope as shown in the left-hand panel of Fig. 4. In order for the intersection between nullclines to yield a set of larger (c_{s}, c) values in the diseased state, parameters would have to be chosen so that the slow nullcline has a positive slope has a positive slope, as in the right-hand panel of Fig. 4.

The SCN modulates not only the input signal $I(t)$, but the activity of the adrenal gland as well. The latter responds to circadian stimuli via the splanchnic nerves that relay synaptic signals from the central nervous system to the peripheral sympathetic neurons. These innervate, among other organs, the adrenal medulla, allowing input from the SCN to be relayed to the adrenal tissues. Thus, another possible way of including circadian responses is to include oscillations in the sensitivity parameter that regulates cortisol release in the adrenal gland, as stimulated by ACTH. Specifically, further analysis would include diurnal periodicity in the production of cortisol, driven by an ad hoc periodic form $h(t)$ so that $\mathrm{d}o/\mathrm{d}t = h(t)a - o$ in Eqs. 1. The two oscillatory responses to the SCN, $h(t)$ and $\alpha \sin(\omega t)$, may be out of phase with each other and could lead to interesting "constructive" and "destructive" interference. Diurnal responses in the HPA axis are also known to depend on age, gender, neuroadaptation, exposure to light, jet-lag, and the use of medication [68–73]. Interindividual variability and/or stochastic fluctuations may also be present. These influences can be incorporated in the analysis by introducing time-dependent parameters, by coupling $I_{\mathrm{circ}}(t) = \alpha \sin(\omega t)$ to environmental stimuli that modulate α and/or ω and introduce possible time-dependent phases, and/or by including random noise to the circa-

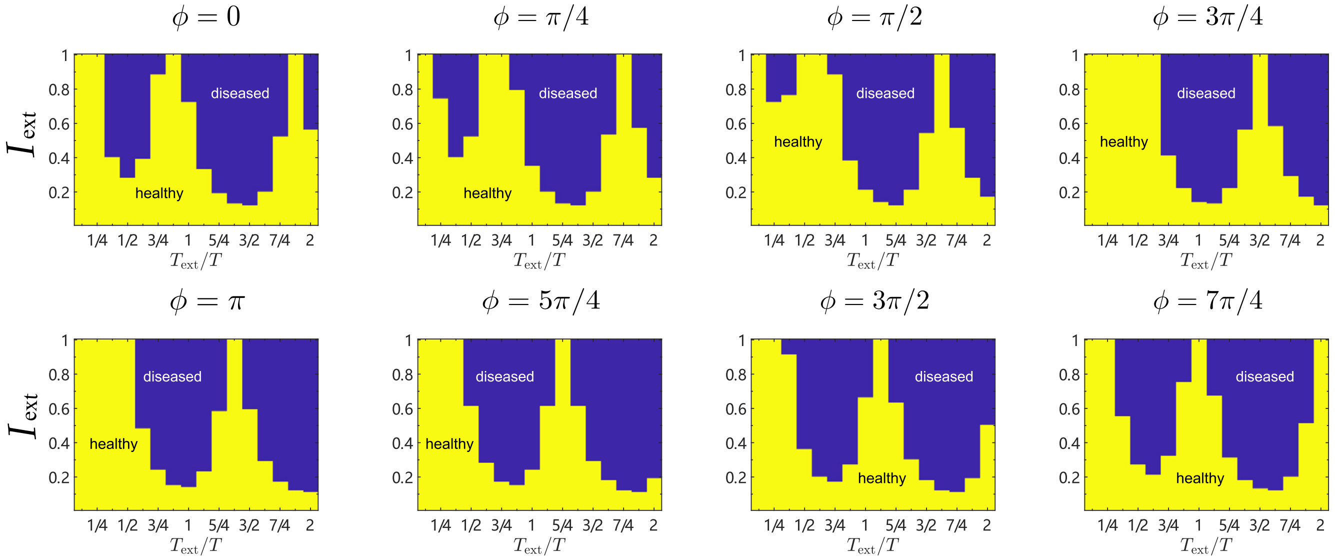

Fig. 14. Starting from a healthy-state limit cycle, we show the final configurations in $\{T_{\rm ext}, I_{\rm ext}\}$ space for $\alpha = 0.02$ and eight values of the start time of the external stress relative to the circadian drive ϕ.

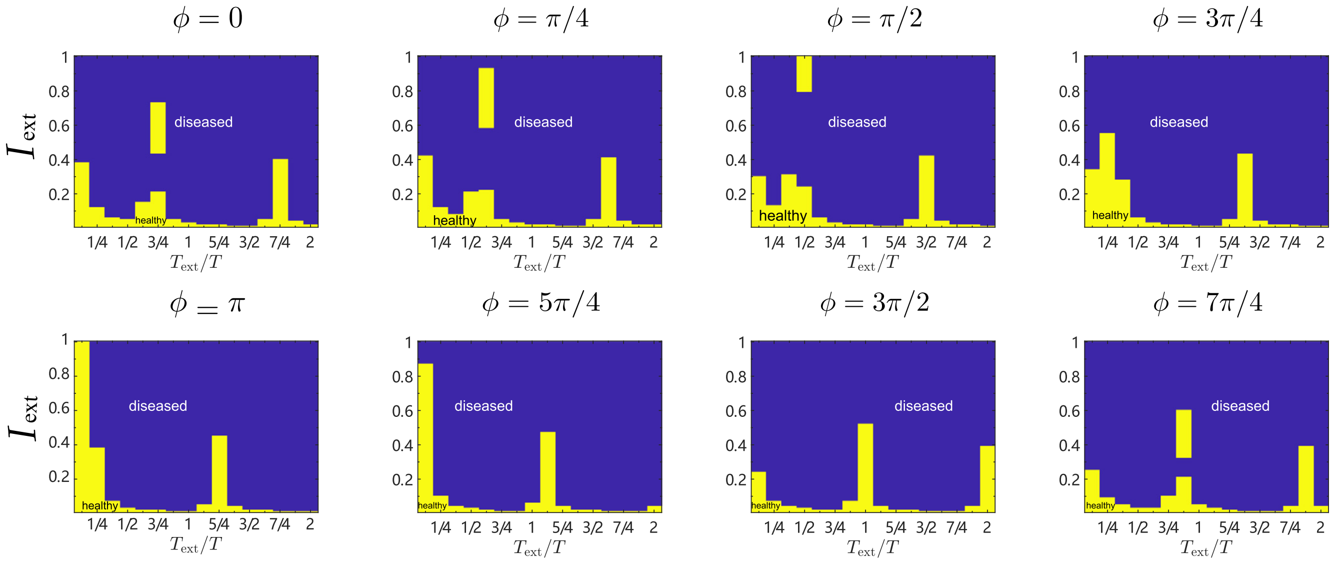

Fig. 15. Starting from a healthy-state limit cycle, we show the final configurations in $\{T_{\rm ext}, I_{\rm ext}\}$ space for $\alpha = 0.03$ and eight values of the start time of the external stress relative to the circadian drive ϕ.

dian amplitude α. Different circadian clock speeds could also be studied following Aschoff's rule, whereby the circadian period T_L is shortened in diurnal mammals exposed to bright, constant light [74]. Conversely, individuals suffering from non-24-h sleep-wake disorder, display abnormally long circadian rhythms, with a period T_D of 25 or 26 h [75]. These scenarios lead to circadian inputs of the type $I_{\rm circ}(t) = \alpha \sin(\omega_{\rm L} t)$ (bright, constant light) and $I_{\rm circ}(t) = \alpha \sin(\omega_D t)$ (sleep-wake disorder) that could be compared to the standard circadian drive $I_{\rm circ}(t) = \alpha \sin(\omega t)$ where $\omega_{\rm L} = 2\pi/T_{\rm L} > \omega$, and $\omega_{\rm D} = 2\pi/T_{\rm D} < \omega$ to investigate how shorter or longer periods affect the dynamics, and the system's response to acute external stressors.

Also of interest is the pineal gland which translates light/dark inputs from the retina into hormonal signals. Specifically, the pineal gland releases melatonin via the activation of beta–adrenergic receptors by norepinephrine to regulate the circadian rhythm. Stress-induced activation of the HPA appears to correlate with an increase in melatonin production [76]; other studies hypothesize that the pineal gland produces CRH-inhibiting factor concomitantly with melatonin, and that melatonin may inhibit production of cortisol in the adrenal gland [77]. Vice-versa, the beta-adregenic receptors of the pineal gland are believed to be sensitive to ACTH concentrations [78]. These findings suggest strong interplay between stress and the circadian system [79], so that a natural extension of our work would be to relate pineal gland and HPA axis dynamics through proper feedback and feedforward equations. Other interesting avenues of research would include analysis of neuroendocrine systems upstream of the HPA axis or more general forms of $I_{\rm ext}(t)$, in the context of control theory. Similarly, environmental stochasticity could also be explored. Preliminary results where α is modeled as a random variable subject to white noise, show that when the noise amplitude is large enough, transitions not previously realized can arise, indicating that external fluctuations may strongly affect the dynamics. Our mechanistic model provides a framework through which therapeutic interventions can be explored, such as cognitive behavioral therapy, often recommended as a first intervention for many psychological disorders.

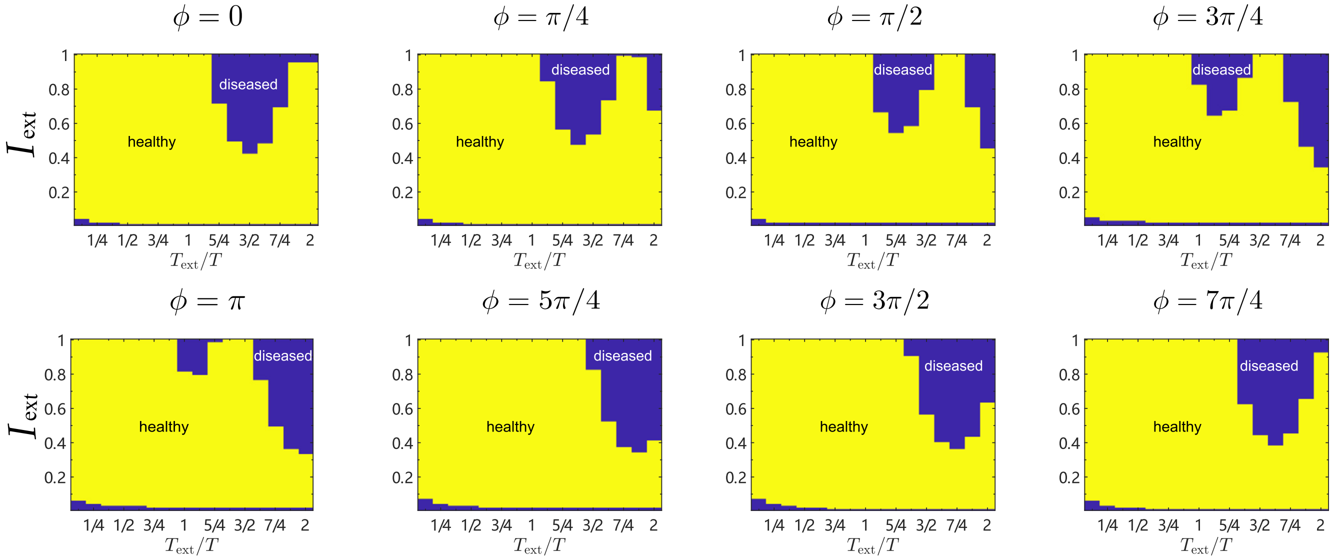

Fig. 16. Starting from a diseased-state limit cycle, we show the final configurations in $\{T_{\rm ext}, I_{\rm ext}\}$ space for $\alpha = 0.01$ and eight values of the start time of the external stress relative to the circadian drive ϕ.

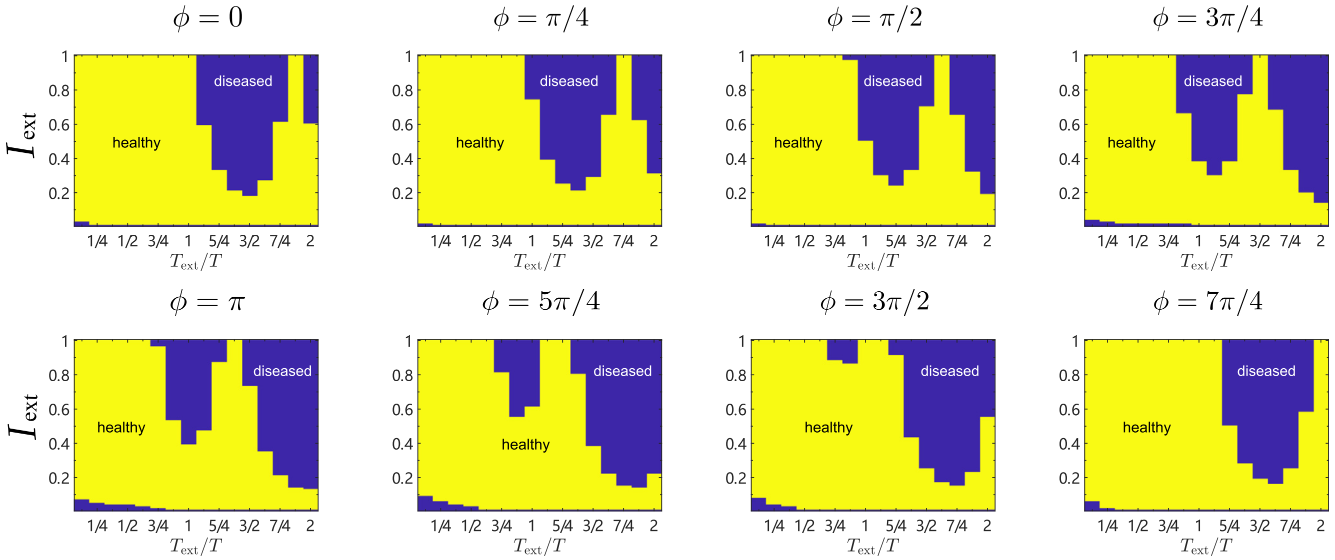

Fig. 17. Starting from a diseased-state limit cycle, we show the final configurations in $\{T_{\rm ext}, I_{\rm ext}\}$ space for $\alpha = 0.02$ and eight values of the start time of the external stress relative to the circadian drive ϕ.

6. Appendix – Linearized model

To better study the dynamics of our specific problem we linearize Eq. 12 by expanding $e^{-bo(y)} = px + q$ as a function of x. This allows us to also formulate a more general system made of two intersecting nullclines: a slow one, given by a vertical line, and a fast one, given by a cubic curve. In this Appendix we study this simplified system as it may serve as a new paradigm for slow-fast bistable dynamical systems. To begin, we write Eqs. 12 and 13 as

$$\frac{dx}{dt} = \varepsilon(x_\infty - x), \tag{56}$$

$$\frac{dy}{dt} = I_0 x - \left(\frac{1}{3}y^3 - \frac{y_1^* + y_2^*}{2}y^2 + y_1^* y_2^* y\right), \tag{57}$$

where $\varepsilon(1-p) \to \varepsilon$, $(\bar{c}_\infty + q)/(1-p) \to x_\infty$. We also rescale $\{x, y, t\} \to \{u, v, t'\}$ and introduce $\bar{\varepsilon}, u_\infty, \gamma$ as follows

$$x = \frac{9}{8I_0}(y_1^* + y_2^*)^3 u, \tag{58}$$

$$y = \frac{3}{2}(y_1^* + y_2^*) v, \tag{59}$$

$$t = \frac{4}{3}(y_1^* + y_2^*)^{-2} t', \tag{60}$$

$$\varepsilon = \frac{3}{4}(y_1^* + y_2^*)^2 \bar{\varepsilon}, \tag{61}$$

$$x_\infty = \frac{9}{8I_0}(y_1^* + y_2^*)^3 u_\infty, \tag{62}$$

$$\gamma = \frac{4}{3} y_1^* y_2^* (y_1^* + y_2^*)^{-2}. \tag{63}$$

We finally arrive at a fundamental form

$$\frac{du}{dt} = \bar{\varepsilon}(u_\infty - u), \tag{64}$$

$$\frac{dv}{dt} = u - \left(v^3 - v^2 + \gamma v\right), \tag{65}$$

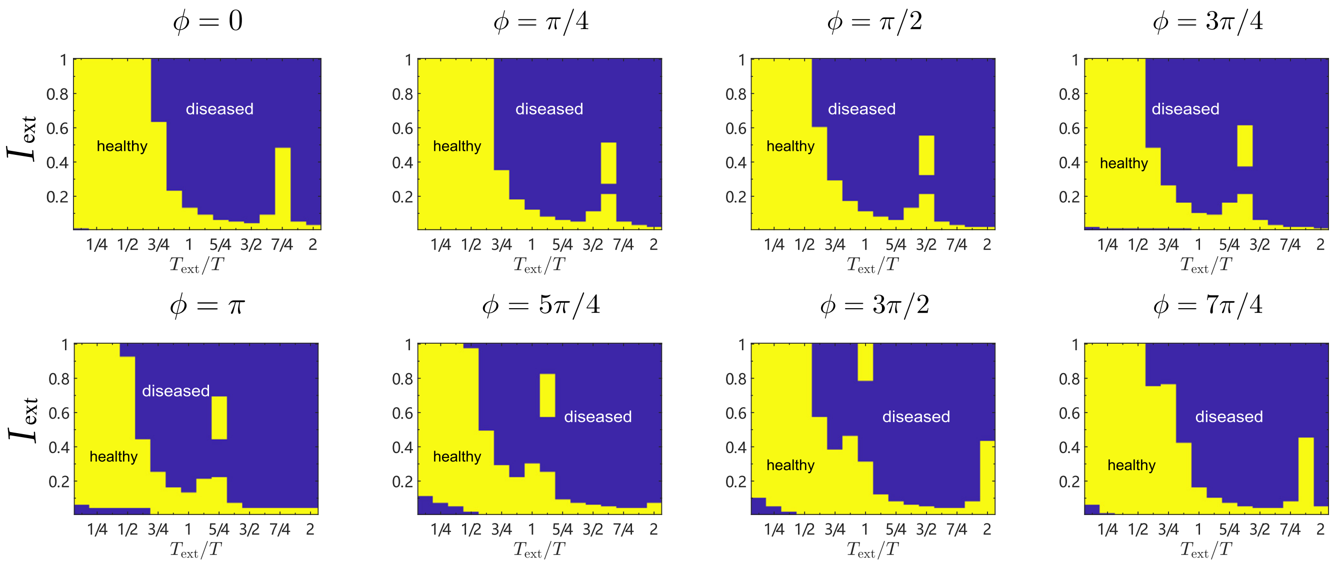

Fig. 18. Starting from a diseased-state limit cycle, we show the final configurations in $\{T_{\rm ext}, I_{\rm ext}\}$ space for $\alpha = 0.03$ and eight values of the start time of the external stress relative to the circadian drive ϕ.

where we dropped the prime notation. The slow u, and fast v nullclines respectively are

$$u = u_\infty, \tag{66}$$

$$u = v^3 - v^2 + \gamma v. \tag{67}$$

The formulation in Eqs. 66 and 67 allows us to better study the dynamics and to classify different behaviors. Along the fast v nullcline the following holds

$$\frac{du}{dv} = 3v^2 - 2v + \gamma, \tag{68}$$

which implies that if $\gamma > 1/3$, the v nullcline is an increasing function of v, and the intersection with the slow u nullcline will yield only one stable fixed-point. Conversely, for $\gamma < 1/3$, the fast v nullcline will have two extrema, located at $v_{1,2} = (1 \pm \sqrt{1-3\gamma})/3$and corresponding to $u_{1,2} = (2\gamma - v_{1,2})v_{1,2}/3$. The (u_1, v_1) and (u_2, v_2) points also represent the turning points of the cubic equation. Note that for $\gamma < 1/3$, if $v_1 < v_2$, then $u_1 > u_2$, and that for $\gamma < 1/4, u_2$ is negative. If $u_\infty > u_1$ or $u_\infty < u_2$ only one stable fixed-point will arise from the intersection of the two nullclines, whereas if $u_2 < u_\infty < u_1$, three intersections exist that yield two stable, fixed-points. We denote these by (u_∞, v_∞^+) and (u_∞, v_∞^-), with $v_\infty^+ > v_\infty^-$. Henceforth, we assume to be in the bistable regime, $u_2 < u_\infty < u_1$. The fast dynamics occurs along the following trajectory

$$\frac{du}{dt} = 0, \tag{69}$$

$$\frac{dv}{dt} = u - (v^3 - v^2 + \gamma v). \tag{70}$$

and thus, initially at least, the system evolves only along the v axis, with u being fixed at its initial condition $u(0)$. By introducing $\tau = \bar{\varepsilon} t$, we can also write the equations that describe the slow dynamics

$$\frac{du}{d\tau} = u_\infty - u \tag{71}$$

$$u = v^3 - v^2 + \gamma v. \tag{72}$$

Since Eq. 71 can be solved analytically, the slow motion along the u axis is

$$u(t) = (u(0) - u_\infty)e^{-\bar{\varepsilon} t} + u_\infty. \tag{73}$$

Upon inserting Eq. 73 in Eq. 72 we can implicitly determine the slow dynamics of $v(t)$

$$v^3 - v^2 + \gamma v = (u(0) - u_\infty)e^{-\bar{\varepsilon} t} + u_\infty. \tag{74}$$

Although trajectories usually move quickly along the v direction, towards the fast v nullcline, for some initial conditions the dynamics may evolve in more subtle ways and additional local analyses may be required. One interesting case is if the initial position is within a small neighborhood of the turning points $(u_{1,2}, v_{1,2})$ of the fast v nullcline. Without loss of generality we focus on the (u_1, v_1) turning point and assume $u(0) = u_1 + \delta u_1(0), v(0) = v_1 + \delta v_1(0)$, with $\delta u_1(0)$ a small perturbation from $u_1, |\delta u_1(0)| \ll u_1$, and similarly $|\delta v_1(0)| \ll v_1$. As per Eqs. 64 and 65, the dynamics is such that if $\delta u_1(0), \delta v_1(0) > 0$ the trajectory will escape the initial neighborhood of the (u_1, v_1) turning point and reach the upper stable fixed-point at (u_∞, v_∞^+). Similarly, if $\delta u_1(0), \delta v_1(0) < 0$ the trajectory will reach the lower stable fixed-point at (u_∞, v_∞^-). Determining the dynamics in other cases depends on the amplitude of $|\delta u_1(0)|, |\delta v_1(0)|$. To be concrete, we assume that $\delta u_1(0) > 0, \delta v_1(0) < 0$. In this case, if $v(t)$ reaches $v = v_1$ before $u(t)$ reaches $u = u_1$, the trajectory will reach the upper stable fixed-point at (u_∞, v_∞^+), whereas if the opposite is true, the lower stable fixed-point at (u_∞, v_∞^-) will be reached. This is depicted in Fig. 19-20, where if the trajectory crosses the blue-dashed boundary it will reach (u_∞, v_∞^-), while if it crosses the red-dashed boundary it will reach (u_∞, v_∞^+). For a given initial condition $u(0) = u_1 + \delta u_1(0), v(0) = v_1 + \delta v_1(0)$ we thus estimate the time $t_{\rm u}^*$ it takes for $u(t_{\rm u}^*) = u_1$, and the time t_v^* it takes for $v(t_v^*) = v_1$, and compare the two to determine which basin of attraction the initial condition belongs to. We begin by studying the dynamics for the slow variable $u(t)$ by writing the solution to Eq. 64 as follows

$$u(t) = u_1 + [(u_1 + \delta u_1(0) - u_\infty)e^{-\bar{\varepsilon} t} + u_\infty - u_1], \tag{75}$$

so that at $t = 0, u(0) = u_1 + \delta u_1(0)$. Note that by writing $u(t) = u_1 + \delta u(t)$ Eq. 75 yields $\delta u(t) = (u_1 + \delta u_1(0) - u_\infty)e^{-\bar{\varepsilon} t} + u_\infty - u_1$. We now pose $v(t) = v_1 + \delta v_1(t)$ and find the time evolu-

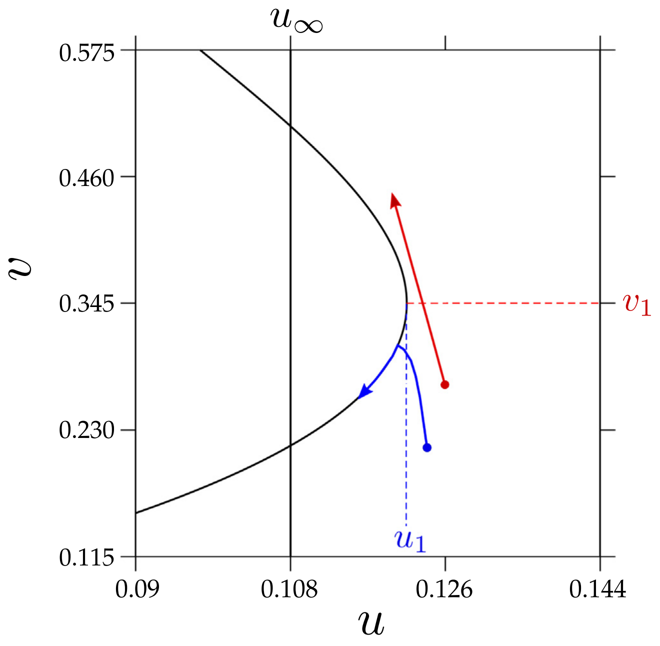

Fig. 19. Detail of the fast nullcline structure in $\{u, v\}$ space near the lower turning point (u_1, v_1). The dynamics of any starting point in the quadrant defined by $u > u_1, v < v_1$ is determined by time t_{v}^* and t_{u}^* trajectories take to the horizontal or vertical lines at $v = v_1$ or $u = u_1$, respectively. For the red initial condition at $(u, v) =, t_{\mathrm{v}} < t_{\mathrm{u}}$ so the trajectory escapes the basin of attraction of the lower equilibrium point at (u_∞, v_∞^-) and eventually reaches the higher equilibrium point at (u_∞, v_∞^+). For the blue initial condition at (u, v)=, $t_{\mathrm{v}} > t_{\mathrm{u}}$ so the trajectory remains in the basin of attraction of the lower equilibrium point and settles at (u_∞, v_∞^-).

tion for $\delta v_1(t)$. Upon inserting Eq. 75 into Eq. 65 and expanding the cubic around (u_1, v_1) we find that $\delta v_1(t)$ obeys the following

$$\frac{\mathrm{d}\delta v_1}{\mathrm{d}t} = (u_1 + \delta u_1(0) - u_\infty)\mathrm{e}^{-\bar{\varepsilon}t} + (1 - 3v_1)\delta v_1^2 - (u_1 - u_\infty). \tag{76}$$

The linear term in δv_1 in Eq. 76 does not contribute to the dynamics, since we are expanding around an extremum of the cubic curve. Also note that $1 - 3v_1 > 0$ and that $u_1 - u_\infty > 0$. We also neglect higher order δv_1^3 terms. Eq. 76 defines a Riccati equation that can be solved by imposing $\delta v_1(t) = -(1 - 3v_1)^{-1} f\prime(t)/f(t)$ and deriving a second order differential equation for $f(t)$. After tedious but straightforward algebra we find that $f(t)$ can be written as a linear combination of Bessel functions and that $\delta v_1(t)$ obeys

$$\delta v_1(t) = \sqrt{\frac{(u_1 + \delta u_1(0) - u_\infty)\mathrm{e}^{-\bar{\varepsilon}t}}{(1 - 3v_1)}}\frac{Y_\nu'(\xi(t)) - HJ_\nu'(\xi(t))}{Y_\nu(\xi(t)) - HJ_\nu(\xi(t))}, \tag{77}$$

where $\nu = 2/\bar{\varepsilon}\sqrt{(u_1 - u_\infty)(1 - 3v_1)}$ and the argument $\xi(t)$ of the J_ν and Y_ν Bessel functions is

$$\xi(t) = \frac{2}{\bar{\varepsilon}}\sqrt{(1 - 3v_1)(u_1 + \delta u_1(0) - u_\infty)\mathrm{e}^{-\bar{\varepsilon}t}}. \tag{78}$$

Finally, the prefactor H is

$$H = \frac{\delta v_1(0)\sqrt{1 - 3v_1}Y_\nu(\xi(0)) - \sqrt{u_1 + \delta u_1(0) - u_\infty}Y_\nu'(\xi(0))}{\delta v_1(0)\sqrt{1 - 3v_1}J_\nu(\xi(0)) - \sqrt{u_1 + \delta u_1(0) - u_\infty}J_\nu'(\xi(0))}. \tag{79}$$

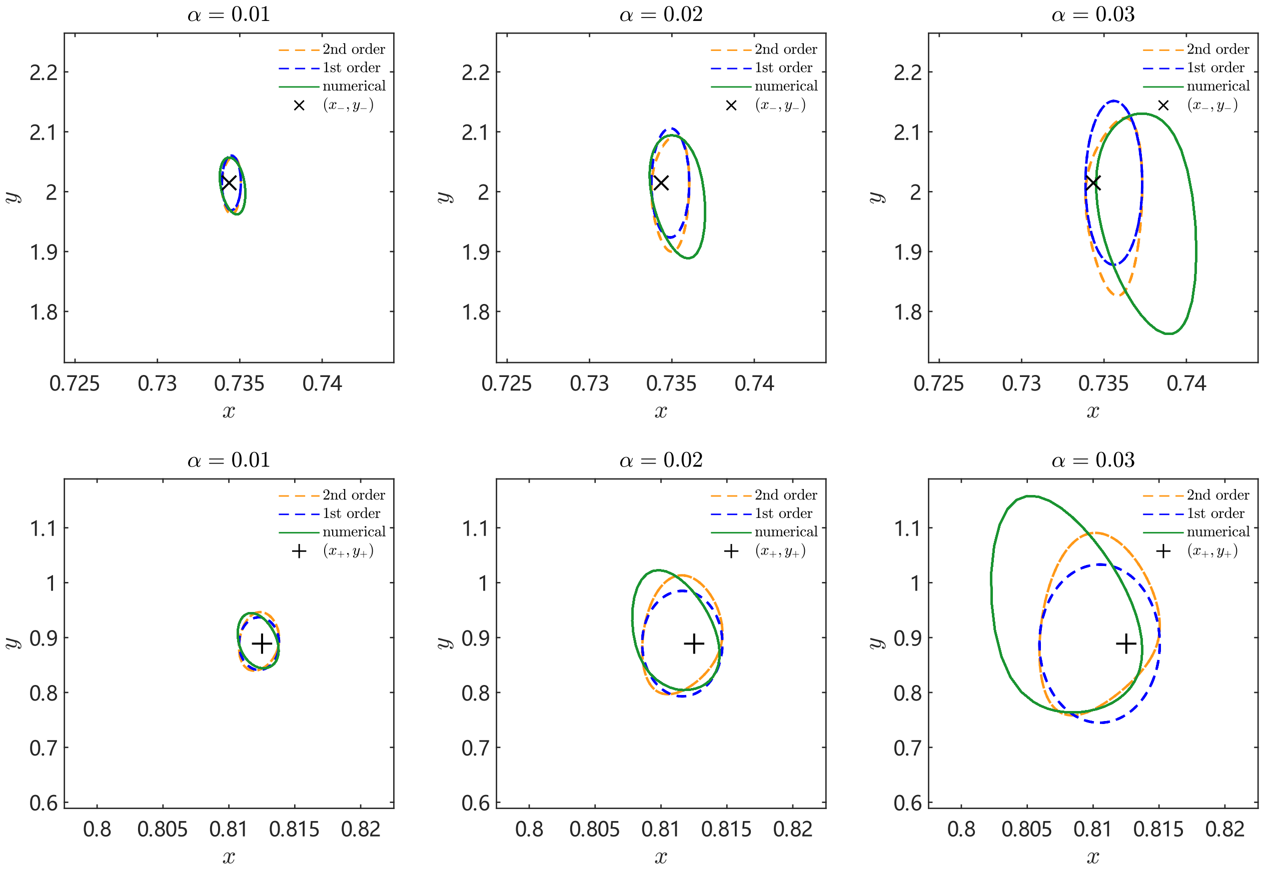

Fig. 20. Periodic orbits in (x, y) space driven by a circadian rhythm of amplitude $\alpha = 0.01, 0.02, 0.03$, from left to right. The green curves represent the exact, numerical solutions obtained from Eqs. 12 and 13; since $x_\alpha^{(1)}(t) = 0$, the blue curves represent analytical approximations up to second order in x with $x_\alpha^{(2)}(t)$ in Eq. 55 and first order in y with $y_\alpha^{(1)}(t)$ given by Eq. 53; the yellow curves represent analytical approximations up to second order in y where $y_\alpha^{(2)}(t)$ given by Eq. 85 is further included. The second order curves typically approximate the exact, numerical solutions with higher accuracy.

The time t_u^* it takes for the trajectory to reach the vertical line at $u = u_1$, from $u(0) = u_1 + \delta u_1(0)$ is given by imposing $\delta u_1(t_u^*) = 0$. From Eq. 75 we find

$$t_u^* = \frac{1}{\varepsilon}\log\left(1 + \frac{\delta u_1(0)}{u_1 - u_\infty}\right). \tag{80}$$

Similarly, the time to reach the horizontal line at $v = v_1$, from $v_1(0) = v_1 + \delta v_1(0)$ is given by imposing $\delta v_1(t_v^*) = 0$. From Eq. 77 we find the implicit expression for t_v^*

$$\frac{Y_v'(\xi(t_v^*))}{J_v'(\xi(t_v^*))} = H \tag{81}$$

Thus, if $t_u^* < t_v^*$ the initial condition will belong to the basin of attraction of the lower fixed-point at (u_∞, v_∞^-), whereas if $t_u^* > t_v^*$ the initial condition will equilibrate at the higher fixed-point at (u_∞, v_∞^+). Finally, the dynamics under initial conditions $\delta u_1(0) < 0$ and $\delta v_1(0) > 0$depend on how $\delta v_1(0)$ compares with $v_{\delta u} - v_1$, where $v_{\delta u}$ is given by

$$u_1 + \delta u_1(0) = v_{\delta u}^3 - v_{\delta u}^2 + \gamma v_{\delta u}. \tag{82}$$

If $v_{\delta u} > v_1$, and $\delta v_1(0) < v_{\delta u} - v_1$, the trajectory will equilibrate at the lower stable fixed-point at (u_∞, v_∞^-). If $\delta v_1(0) > v_{\delta u} - v_1$, the explicit time dependence of the trajectory must be evaluated.

7. Appendix - Higher order solutions to the circadian problem

In this Appendix we find $y_\alpha^{(2)}(t)$, the second order solution in α to the circadian problem presented in Eqs. 12 and 13 as driven by Eq. 32. We thus solve Eq. 48 and, for simplicity, specifically seek periodic solutions. To this end, we set the proper initial conditions so that only oscillatory terms arise from Eq. 48. Upon inserting Eqs. 53 and 55 into Eq. 48, with $x_\alpha^{(1)} = 0$, we obtain

$$\frac{\mathrm{d}y_\alpha^{(2)}}{\mathrm{d}t} = -\sigma y_\alpha^{(2)} + B\sin(\omega t) + C\cos(\omega t) + D\cos(2\omega t) + E\sin(2\omega t) + F \tag{83}$$

where

$$\begin{aligned}
B &= I_0 M x_{\mathrm{u}} bo'(y_{\mathrm{u}})\mathrm{e}^{-bo(y_{\mathrm{u}})}\frac{\omega}{\omega(\omega^2+\sigma^2)},\\
C &= I_0 M x_{\mathrm{u}} bo'(y_{\mathrm{u}})\mathrm{e}^{-bo(y_{\mathrm{u}})}\frac{\sigma}{\omega(\omega^2+\sigma^2)},\\
D &= -x_{\mathrm{u}}^2\left(y_{\mathrm{u}} - \frac{y_1^*+y_2^*}{2}\right)\frac{\omega^2-\sigma^2}{2(\omega^2+\sigma^2)^2},\\
E &= x_{\mathrm{u}}^2\left(y_{\mathrm{u}} - \frac{y_1^*+y_2^*}{2}\right)\frac{2\omega\sigma}{2(\omega^2+\sigma^2)^2},\\
F &= I_0 x_\alpha^{(2)}(0) - I_0 M bo'(y_{\mathrm{u}})\mathrm{e}^{-bo(y_{\mathrm{u}})}\frac{x_{\mathrm{u}}\sigma}{\omega(\omega^2+\sigma^2)}\\
&\quad -\left(y_{\mathrm{u}} - \frac{y_1^*+y_2^*}{2}\right)\frac{x_{\mathrm{u}}^2}{2(\omega^2+\sigma^2)}.
\end{aligned} \tag{84}$$

and where $\sigma = (y_{\mathrm{u}} - y_1^*)(y_{\mathrm{u}} - y_2^*)$. Thus,

$$\begin{aligned}
y_\alpha^{(2)}(t) = &\left(y_\alpha^{(2)}(0) + \frac{\omega B}{\omega^2+\sigma^2} - \frac{\sigma C}{\omega^2+\sigma^2} + \frac{2\omega E}{4\omega^2+\sigma^2} - \frac{\sigma D}{4\omega^2+A^2} - \frac{F}{\sigma}\right)\mathrm{e}^{-\sigma t}\\
&+\left(\frac{\sigma C}{\omega^2+\sigma^2} - \frac{\omega B}{\omega^2+\sigma^2}\right)\cos(\omega t) + \left(\frac{\sigma B}{\omega^2+\sigma^2} + \frac{\omega C}{\omega^2+\sigma^2}\right)\sin(\omega t)\\
&+\left(\frac{\sigma D}{4\omega^2+\sigma^2} - \frac{2\omega E}{4\omega^2+\sigma^2}\right)\cos(2\omega t)\\
&+\left(\frac{2\omega D}{4\omega^2+\sigma^2} + \frac{\sigma E}{4\omega^2+\sigma^2}\right)\sin(2\omega t) + \frac{F}{\sigma}.
\end{aligned} \tag{85}$$

To obtain a purely oscillatory solution we impose that the $e^{-\sigma t}$ prefactor be zero, so that

$$y_\alpha^{(2)}(0) = -\frac{B\omega}{\omega^2+\sigma^2} + \frac{\sigma C}{\omega^2+\sigma^2} - \frac{2\omega E}{4\omega^2+\sigma^2} + \frac{\sigma D}{4\omega^2+\sigma^2} + \frac{F}{\sigma}. \tag{86}$$

We also determine the value of $x_\alpha^{(2)}(0)$ that should be used as the proper initial condition to Eq. 55 if one is seeking a pure oscillatory solution to order α^3. We thus derive the time dynamics for $x_\alpha^{(3)}(t)$

$$\begin{aligned}
\frac{\mathrm{d}x_\alpha^{(3)}}{\mathrm{d}t} = &-Mbo'(y_{\mathrm{u}})\mathrm{e}^{-bo(y_{\mathrm{u}})}y_\alpha^{(2)}\\
&+\frac{M}{2}\mathrm{e}^{-bo(y_{\mathrm{u}})}\left(b^2(o'(y_{\mathrm{u}}))^2 - bo''(y_{\mathrm{u}})\right)(y_\alpha^{(1)})^2 - Mx_\alpha^{(2)}.
\end{aligned} \tag{87}$$

After inserting Eqs. 53, 55 and 85 with $x_\alpha^{(1)} = 0$ into Eq. 87, we set the resulting constant term in the right-hand side to zero, so that upon integration of Eq. 87 there are no linear terms and $x_\alpha^{(3)}$ is purely periodic. After some algebraic manipulations we find

$$\begin{aligned}
x_\alpha^{(2)}(0) = &\frac{1}{\sigma\mathrm{e}^{bo(y_{\mathrm{u}})} + bo'(y_{\mathrm{u}})I_0}\Bigg[\frac{x_{\mathrm{u}}^2\sigma}{4(\omega^2+\sigma^2)}\left(b^2(o'(y_{\mathrm{u}}))^2 - bo''(y_{\mathrm{u}})\right)\\
&+ M\frac{x_{\mathrm{u}}\sigma^2 bo'(y_{\mathrm{u}})}{\omega(\omega^2+\sigma^2)} + \frac{x_{\mathrm{u}}bo'(y_{\mathrm{u}})}{\omega(\omega^2+\sigma^2)}(I_0 Mbo'(y_{\mathrm{u}})\mathrm{e}^{-bo(y_{\mathrm{u}})}\sigma\\
&+\frac{x_{\mathrm{u}}y_{\mathrm{u}}\omega}{2} - \frac{x_{\mathrm{u}}\omega(y_1^*+y_2^*)}{4})\Bigg]
\end{aligned} \tag{88}$$

8. Appendix - Numerical comparisons between first and second order approximations

In this section we show the difference between lower (first) and higher (second) order approximations to the limit cycles in (x, y) space driven by the circadian rhythm $I_{\mathrm{circ}}(t) = \alpha\sin(\omega t)$ where $\alpha = 0.01, 0.02, 0.03$. In Fig. 20, the exact, numerical solutions obtained from Eqs. 12 and 13 are shown in green; since $x_\alpha^{(1)}(t) = 0$, second order approximations of $x(t)$ upto $x_\alpha^{(2)}(t)$ from Eq. 55 and first order approximations of $y(t)$ upto $y_\alpha^{(1)}(t)$ from Eq. 53 are depicted in blue, and second order approximations both in x and y, with $y_\alpha^{(2)}(t)$ from Eq. 85 further included are plotted in yellow. Second order curves typically approximate the exact, numerical solutions with higher accuracy.

9. Appendix - Stored CRH dynamics as the smallest perturbation

We now explore numerical solutions for values of $\alpha > 0.03$ where period-doubling, subharmonics, and chaotic behavior emerge. Unless specified, all parameters are chosen as in Section 3.1, 3.2 and Table 1 with initial conditions set at $(x(0), y(0)) = (x_+, y_+)$. Henceforth all of our numerical integration will be performed using ode45 in MATLAB®. Before illustrating our results, we note that the circadian version of Eqs. 12 and 13, where $I_0 \to I_0 + \alpha\sin(\omega t)$, is reminiscent of the well known Duffing oscillator, characterized by a periodic forcing term and nonlinear elasticity [80]. The Duffing oscillator displays period doubling, other subharmonic responses, and chaos, as the amplitude of the forcing term is varied. These features arise from the nonlinear elasticity, so that a forcing term of period T may yield a response of augmented period mT, where m is an integer. The case $m = 2$ represents period-doubling. Other values of m are subharmonic responses of order $1/m$, whereas very large values of m are associated to chaos. Our circadian system is more complicated than the Duffing oscillator, however, inertia, nonlinear terms and periodic forcing are similarly present. One key parameter is α, the prefactor of the circadian term and the equivalent of the amplitude of the

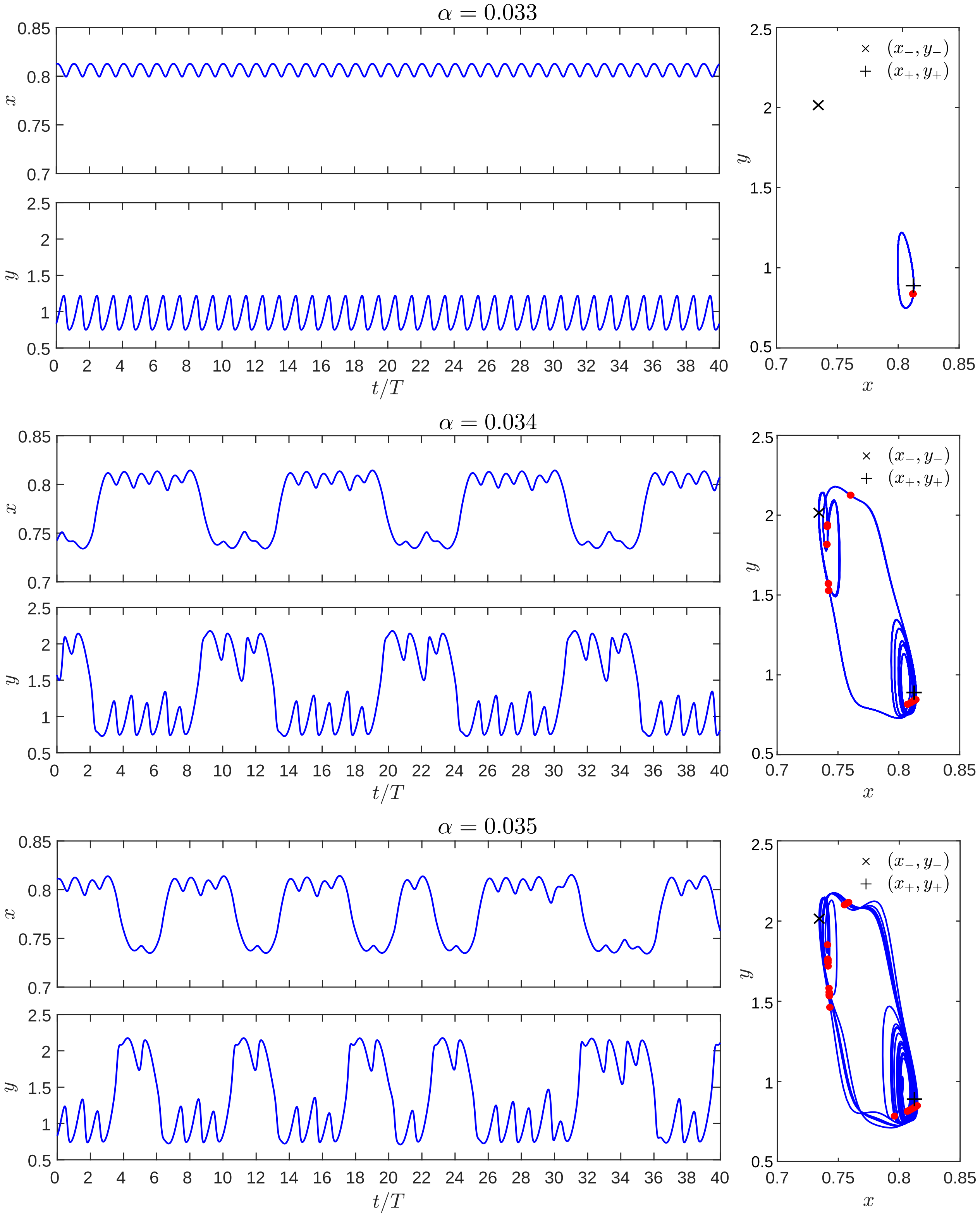

Fig. 21. Time series and phase portraits from Eqs. 12 and 13 driven by $I(t) = I_0 + \alpha\sin(\omega t)$ for $\alpha = 0.033, 0.034, 0.035$. Other parameters are listed in Sect. 3.1, 3.2 and Table 1. The red dots in the phase portraits indicate times that are integer multiples of $T = 2\pi/\omega$. Periods are T ($\alpha = 0.033$), and $11T$ ($\alpha = 0.034$). Chaos emerges at $\alpha = 0.035$.

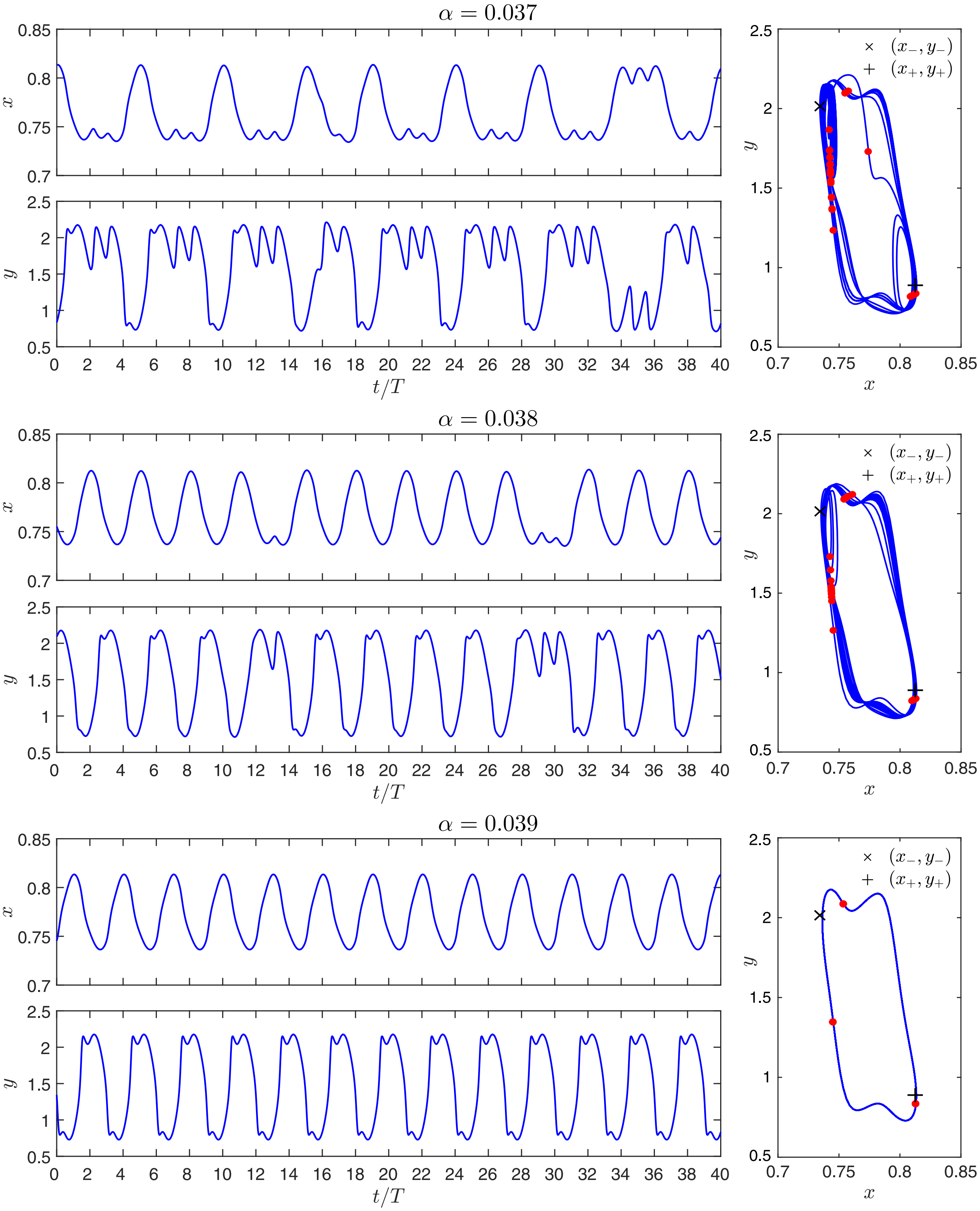

Fig. 22. Time series and phase portraits from Eqs. 12 and 13 driven by $I(t) = I_0 + \alpha\sin(\omega t)$ for $\alpha = 0.037, 0.038, 0.039$. Other parameters are listed in Sect. 3.1, 3.2 and Table 1. The red dots in the phase portraits indicate times that are integer multiples of $T = 2\pi/\omega$. Chaotic trajectories arise for $\alpha = 0.037, 0.038$. For $\alpha = 0.039$, the period is $3T$.

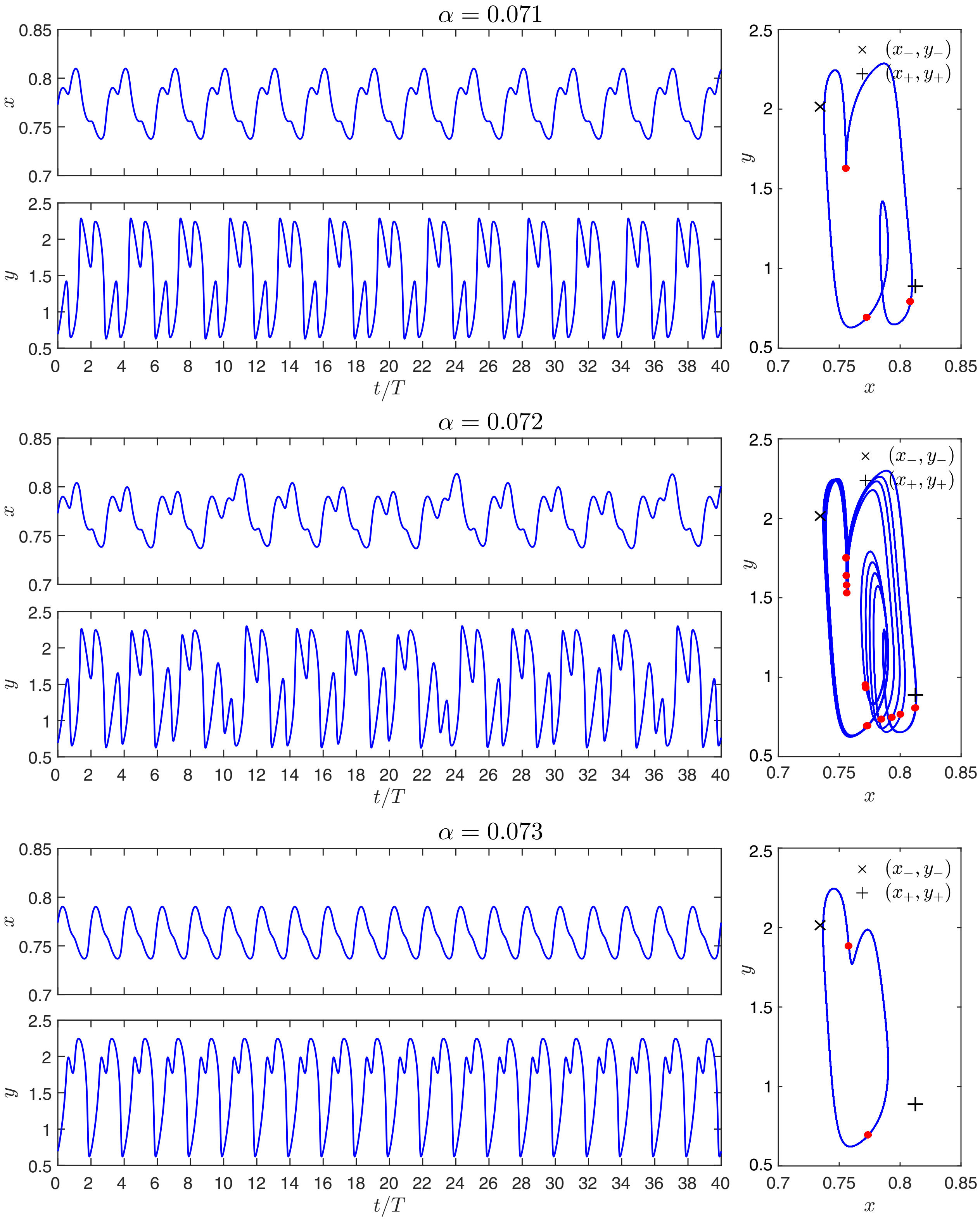

Fig. 23. Time series and phase portraits from Eqs. 12 and 13 driven by $I(t) = I_0 + \alpha \sin(\omega t)$ for $\alpha = 0.071, 0.072, 0.073$. Other parameters are listed in Sect.,3.1, 3.2 and Table 1. The red dots in the phase portraits indicate times that are integer multiples of $T = 2\pi/\omega$. Periods are $3T$ ($\alpha = 0.071$), $13T$ ($\alpha = 0.072$), and $2T$ ($\alpha = 0.073$).

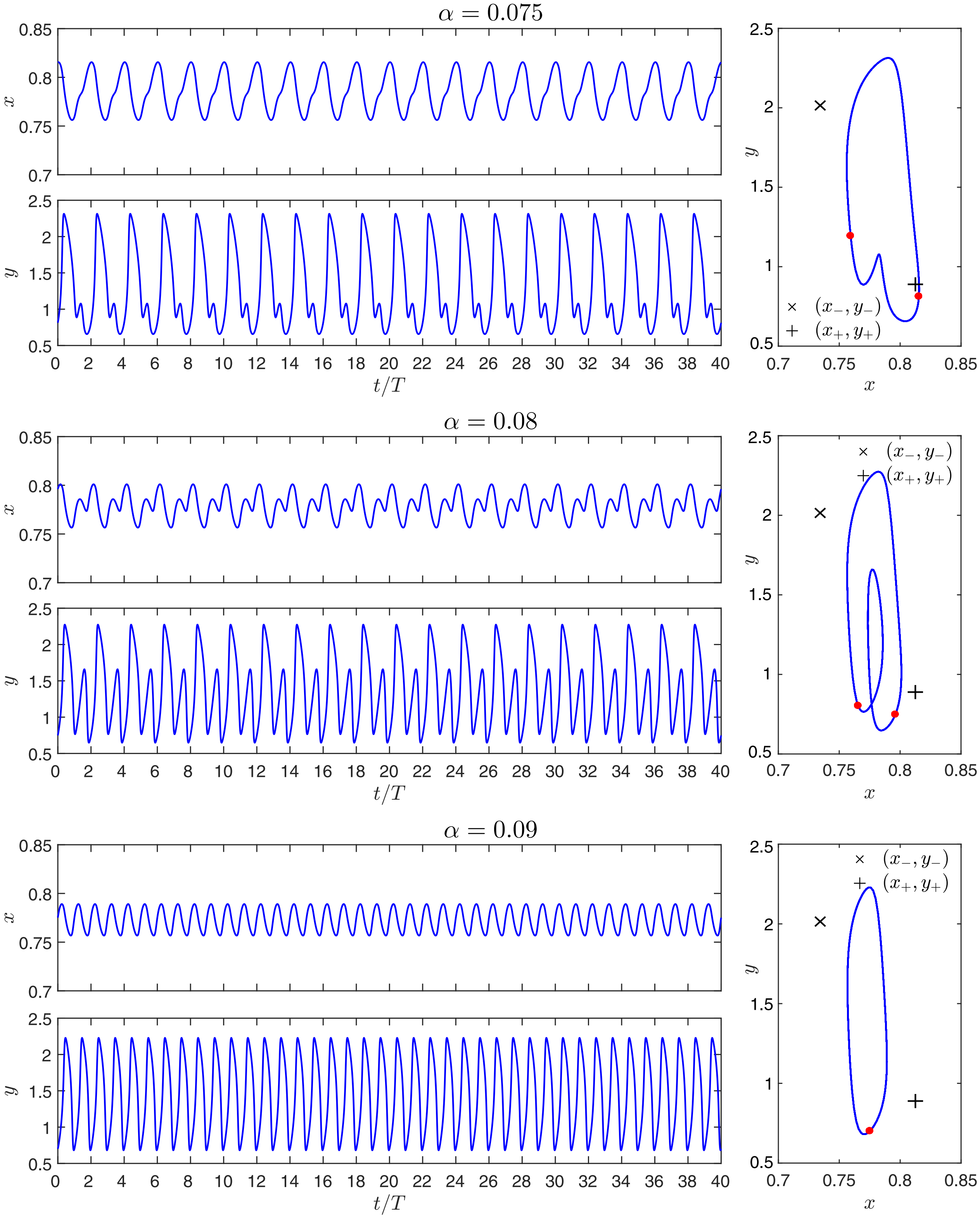

Fig. 24. Time series and phase portraits from Eqs. 12 and 13 driven by $I(t) = I_0 + \alpha \sin(\omega t)$ for $\alpha = 0.075, 0.08, 0.09$. Other parameters are listed in Sect.,3.1, 3.2 and Table 1. The red dots in the phase portraits indicate times that are integer multiples of $T = 2\pi/\omega$. Periods are $2T$ ($\alpha = 0.075$), $2T$ ($\alpha = 0.08$), and T ($\alpha = 0.09$).

forcing term in the Duffing oscillator. We find that increasing α leads to the emergence of period-doubling bifurcations, subharmonics, and chaos in the circadian version of Eqs. 12 and 13, just as for the Duffing oscillator.

In Figs. 21–24 we plot the time series $x(t)$ and $y(t)$ and the phase portraits (x, y) as derived from Eqs. 12 and 13 with $I_0 \rightarrow I_0 + \alpha\sin(\omega t)$, for increasing values of $\alpha > 0.03$. All trajectories are initiated at the steady state $(x_u, y_u) = (x_+, y_+)$ of the reduced model Eqs. 12 and 13 without the circadian term. We let the system run for $t = 200T$ and then reset the clock, following the dynamics for a further $t = 40T$ period. Since we are interested in the long term dynamics, we only plot the trajectories during the final $t = 40T$ period and do not show the initial $t = 200T$ transient. The sole exceptions are the chaotic cases $\alpha = 0.035, 0.037, 0.038$ in Figs. 21 and 22 where the transient is set at $t = 500T$. The red dots in Figs. 21–24 represent the Poincaré section, the discrete set of points in phase space at times $t = mT$. If the response is a simple periodic orbit the Poincaré section is a single point; after a period-doubling bifurcation, the Poincaré section consists of two points, representing doubling of the periodicity. For a subharmonic response of order $1/m$, the Poincaré section consists of m points, indicating that the period is increased by a factor m with respect to the circadian term. Chaos leads to a richer set of points in the Poincaré section. Chaotic behavior arises for $0.035 \leqslant \alpha \leqslant 0.038$ as can be seen in Figs. 21 and 22. In Fig. 23 we find a $1/3$ subharmonic with period $3T$ for $\alpha = 0.071$. The limit cycle passes in the vicinity of both (x_-, y_-) and (x_+, y_+) and crosses itself. A slight increase to $\alpha = 0.072$ leads to a $1/13$ subharmonic with period $13T$, yet further increases to $\alpha = 0.073$ result in period-doubling with the emergence of limit cycle of period $2T$. Finally, in Fig. 24 we observe the limit cycle acquiring simpler periodic forms from $\alpha = 0.075$ to $\alpha = 0.09$. In Appendix 10 we show chaotic phase portraits for $0.035 \leqslant \alpha \leqslant 0.038$ over a much longer time frame, up to $t = 10,000T$. We also tested both lower accuracy (ode23) and higher accuracy (smaller time step-sizes and stricter tolerances for absolute and relative errors) methods to verify that chaotic behavior is an intrinsic feature of the dynamics and not an artifact of our numerical computation.

10. Appendix – Chaotic phase portraits

In Fig. 25 we show the chaotic phase portraits and the Poincaré maps arising from Eqs. 12 and 13 driven by the circadian term $I_0 + \alpha\sin(\omega t)$ for $0.035 \leqslant \alpha \leqslant 0.038$. All other parameters are chosen as in Sect. 3.2, Appendix 9 and Table 1. The initial condition is

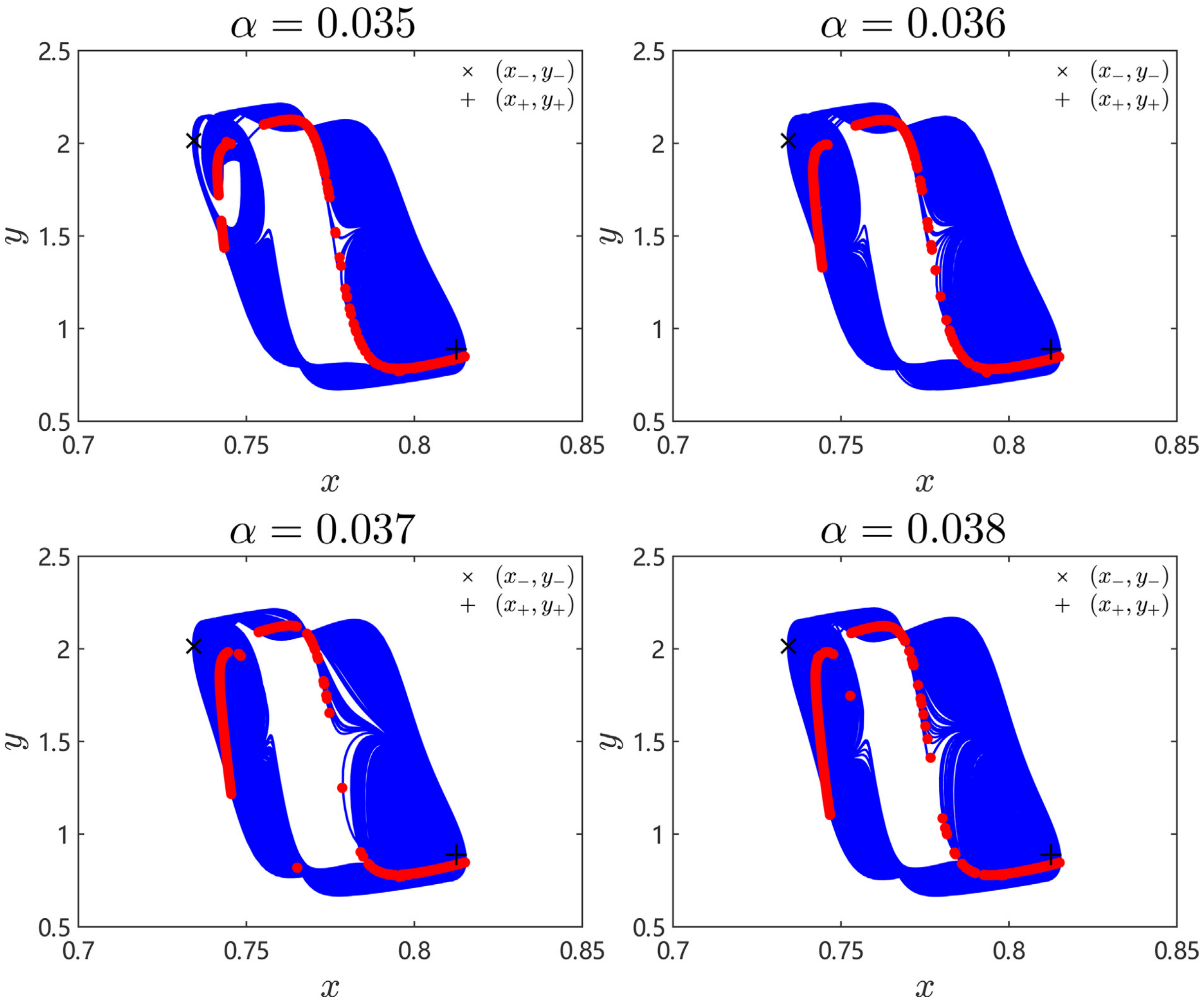

Fig. 25. Phase portraits in (x, y) space arising from Eqs. 12 and 13 driven by $I(t) = I_0 + \alpha\sin(\omega t)$ for $0.035 \leqslant \alpha \leqslant 0.038$. The initial transient is not shown. Numerical evaluations are carried out up to 10,000T. Each red dot represents times that are integer multiples of $T = 2\pi/\omega$ indicating chaotic behavior.

set at $(x_u, y_u) = (x_+, y_+)$ of the reduced problem Eqs. 12 and 13 without the circadian drive. As described in Appendix 9 we let the system run for $t = 500T$ and then reset the clock, following the dynamics for an additional $t = 10,000T$. We do not show the initial $t = 500T$ transient in any of the panels in Fig. 25 but follow the dynamics over the subsequent $t = 10,000T$. There is no limiting period over the $t = 10,000T$ timeframe.

Declaration of Competing Interests

The authors declare that they have no known competing financial interests or personal relationships that could have appeared to influence the work reported in this paper.

Acknowledgements

This work was partially supported by the elite undergraduate training program of School of Mathematical Sciences in Peking University (XC), grants from the Army Research Office through grant W911NF-18–1-0345 and the NSF through grants DMS-1814364 (TC) and DMS-1814090 (MD).

References

[1] Yehuda R. Post-traumatic stress disorder. N Engl J Med 2002;346:108–14.

[2] Herman JP, McKlveen JM, Ghosal S, Kopp B, Wulsin A, Makinson R, Scheimann J, Myers B. Regulation of the hypothalamic-pituitary-adrenocortical stress response. Comprehensive Physiol 2016;6:603–21.

[3] Strand FL. Neuropeptides: Regulators of Physiological Processes. MIT Press; 1999.

[4] Thun R, Eggenberger E, Zerobin K, LÜscher T, Vetter W. Twenty-four-hour secretory pattern of cortisol in the bull. Endocrinology 1981;109:2208–12.

[5] Veldhuis JD, Iranmanesh A, Lizarralde G, Johnson ML. Amplitude modulation of a burstlike mode of cortisol secretion subserves the circadian glucocorticoid rhythm. Am J Physiol 1989;257:E6–E14.

[6] Mershon JL, Sehlhorst CS, Rebar RW, Liu JH. Evidence of a corticotropin-releasing hormone pulse generator in the macaque hypothalamus. Endocrinology 1992;130:2991–6.

[7] Engler O, Pham T, Fullenon TM, Ooi G, Funder JW, Clarke IJ. Studies of the secretion of corticotropin releasing factor and arginine vasopressin into hypophyseal portal circulation of the conscious sheep. Neuroendocrinology 1989;49:367–81.

[8] Trifonova ST, Gantenbein M, Turner JD, Muller CP. The use of saliva for assessment of cortisol pulsatile secretion by deconvolution analysis. Psychoneuroendocrinology 2013;38:1090–101.

[9] Spiga F, Walker JJ, Terry JR, Lightman SL. HPA axis rhythms. Comprehensive Physiol 2014;4:1273–98.

[10] Engler D, Pham T, Liu J, Fullerton M, Clarke I, Funder J. Studies of the regulation of the hypothalamic-pituitary-adrenal axis in sheep with hypothalamic-pituitary disconnection. II. Evidence for in vivo ultradian hypersecretion of proopiomelanocortin peptides by the isolated anterior and intermediate pituitary. Endocrinology 1990;127:1956–66.

[11] Melmed S. The pituitary. London, UK: Academic Press; 2011.

[12] Smith SM, Vale WW. The role of the hypothalamic-pituitary-adrenal axis in neuroendocrine responses to stress. Dialogues Clin Neurosci 2006;8:383–95.

[13] Nemeroff CB et al. Elevated concentration of CSF corticotropin-releasing factor-like immunoreactivity in depressed patients. Science 1984;226:1342–4.

[14] Banki CM, Bissette G, Arato M, O'Connor L, Nemeroff CB. CSF corticotropin-releasing factor-like immunoreactivity in depression and schizophrenia. Am J Psychiatry 1987;144:873–7.

[15] Holsboer F. The corticosteroid receptor hypothesis of depression. Neuropsychopharmacology 2000;23:477–501.

[16] Claes SJ. CRH, stress, and major depression: a psychobiological interplay. In: Litwack G, editor. Vitamins and hormones, vol. 69. Elsevier Academic Press; 2004. p. 117–50.

[17] Parrish Waters R, Rivalan M, Bangasser DA, Deussing JM, Ising M, Wood SK, Holsboer F, Summers CH. Evidence for the role of corticotropin-releasing factor in major depressive disorder. Neurosci Biobehav Rev 2015;58:63–78.

[18] Hotta M, Shibasaki T, Masuda A, Imaki T, Demura H, Ling N, Shizume K. The responses of plasma adrenocorticotropin and cortisol to corticotropin-releasing hormone (CRH) and cerebrospinal fluid immunoreactive CRH in anorexia nervosa patients. J Clin Endocrinol Metabol 1986;62:319–24.

[19] Warren MP. Endocrine manifestations of eating disorders. J Clin Endocrinol Metabol 2011;96:333–43.

[20] Miller KK. Endocrine effects of anorexia nervosa. Endocrinol Metab Clin North Am 2013;42:515–28.

[21] Nandam LS, Brazel M, Zhou M, Jhaveri DJ. Cortisol and major depressive disorder – translating findings from humans to animal models and back. Front Psychiatry 2020;10:974.

[22] Williams WC, Island D, Oldfield RA, Grant GW. Blood corticotropin (ACTH) levels in Cushing's disease. J Clin Endocrinol Metabol 1961;21:426–32.

[23] van den Berg G, Pincus SM, Veldhuis JD, Frölich M, Roelfsema F. Greater disorderliness of ACTH and cortisol release accompanies pituitary-dependent Cushing's disease. Eur J Endocrinol 1997;136:394–400.

[24] Barber TM, Adams E, Ansorge O, Byrne JV, Karavitaki N, Wass JAH. Nelson's syndrome. Eur J Endocrinol 2010;163:495–507.

[25] Patel J, Eloy JA, Liu JK. Nelson's syndrome: a review of the clinical manifestations, pathophysiology, and treatment strategies. Neurosurg Focus 2015;38:E14.

[26] Kelestimur F. Sheehan's syndrome. Pituitary 2003;6:181–8.

[27] Raff H, Sharma ST, Nieman LK. Physiological basis for the etiology, diagnosis, and treatment of adrenal disorders: Cushing's syndrome, adrenal insufficiency, and congenital adrenal hyperplasia. Comprehensive Physiol 2014;4:739–69.

[28] DeMorrow S. Role of the hypothalamic-pituitary-adrenal axis in health and disease. Int J Mol Sci 2018;19:986.

[29] Dienes KA, Hazel NA, Hammen CL. Cortisol secretion in depressed and at-risk adults. Psychoneuroendocrinology 2013;38:927–40.

[30] Yehuda R, Southwick SM, Nussbaum G, Wahby V, Giller EL, Mason JW. Low urinary cortisol excretion in patients with post-traumatic stress disorder. J Nervous Mental Dis 1990;178:366–9.

[31] Yehuda R, Bierer LM, Schmeidler J, Aferiat DH, Breslau I, Dolan S. Low cortisol and risk for PTSD in adult offspring of holocaust survivors. Am J Psychiatry 2000;157:1252–9.

[32] Yehuda R. Current status of cortisol of findings in post-traumatic stress disorder. Psychiatr Clin North Am 2002;25:341–68.

[33] Yehuda R, Golier JA, Kafman S. Circadian rhythm of salivary cortisol in Holocaust survivors with and without PTSD. Am J Psychiatry 2005;162:998–1000.

[34] Wessa M, Rohleder N, Kirschbaum C, Flor H. Altered cortisol awakening response in posttraumatic stress disorder. Psychoneuroendocrinology 2006;31:209–15.

[35] Weems C, Carrion V. The association between PTSD symptoms and salivary cortisol in youth: The role of time since the trauma. J Trauma Stress 2007;20:903–7.

[36] Gill J, Vythilingam M, Page GG. Low cortisol, high DHEA, and high levels of stimulated TNF-α) and IL-6 in women with PTSD. J Trauma Stress 2006;21:530–9.

[37] Delaney E. The relationship between traumatic stress, PTSD and cortisol. Naval Center for Combat & Operational Stress Control Publication, Navy Bureau of Medicine and Surgery 2010.

[38] Morris MC, Compas BE, Garber J. Relations among post–traumatic stress disorder, co-morbid major depression, and HPA function: a systematic review and meta-analysis. Clin Psychol Rev 2012;32:301–15.

[39] Wahbeh H, Oken BS. Salivary cortisol lower in posttraumatic stress disorder. J Trauma Stress 2013;11:1–15.

[40] Nieman LK, Chanco Turner ML. Addison's disease. Clin Dermatol 2006;24:276–80.

[41] Ouanes S, Popp J. High cortisol and the risk of dementia and Alzheimer's disease: a review of the literature. Front Aging Neurosci 2019;11:43.

[42] Vandael D, Gounko NV. Corticotropin releasing factor-binding protein (CRF-BP) as a potential new therapeutic target in Alzheimer's disease and stress disorders. Transl Psychiatry 2019;9:272.

[43] Klaassens ER, Giltay EJ, Cuijpers P, van Veen T, Zitman FG. Adulthood trauma and HPA-axis functioning in healthy subjects and PTSD patients: a meta-analysis. Psychoneuroendocrinology 2012;37:317–31.

[44] Kyrylov V, Severyanova L, Vieira A. Modeling robust oscillatory behavior of the hypothalamic-pituitary-adrenal axis. IEEE Trans Biomed Eng 2005;52:1977–83.

[45] Jelic S, Cupic Z, Kolar-Anic L. Mathematical modeling of the hypothalmic-pituitary-adrenal system activity. Math Biosci 2005;197:173–87.

[46] Savić D, Jelić S. A mathematical model of the hypothalamo-pituitary-adrenocortical system and its stability analysis. Chaos Solitons Fractals 2005;26:427–36.

[47] Gupta S, Aslakson E, Gurbaxani BM, Vernon SD. Inclusion of the glucocorticoid receptor in a hypothalamic pituitary adrenal axis model reveals bistability. Theor Biol Med Modell 2007;4:8.

[48] Vinther F, Andersen M, Ottesen JT. The minimal model of the hypothalamic-pituitary-adrenal axis. J Math Biol 2011;63:663–90.

[49] Sriram K, Rodriguez-Fernandez M, Doyle III FJ. Modeling cortisol dynamics in the neuro-endocrine axis distinguishes normal, depression, and post-traumatic stress disorder (PTSD) in humans. PLoS Comput Biol 2012;8: e1002379.

[50] Rankin J, Walker J, Windle R, Lightman S, Terry J. Characterizing dynamic interactions between ultradian glucocorticoid rhythmicity and acute stress using the phase response curve. PloS One 2012;7: e30978.

[51] Andersen M, Vinther F, Ottesen J. Mathematical modeling of the hypothalamic-pituitary-adrenal gland (HPA) axis, including hippocampal mechanisms. Math Biosci 2013;246:122–38.

[52] Walker JJ, Spiga F, Gupta R, Zhao Z, Lightman SL, Terry JR. Rapid intra-adrenal feedback regulation of glucocorticoid synthesis. J R Soc Interface 2015;12:20140875.

[53] Savić D, Knežević G, Opačić G. A mathematical model of stress reaction: Individual differences in threshold and duration. Psychobiology 2000;28:581–92.

[54] Walker JJ, Terry JR, Lightman SL. Origin of ultradian pulsatility in the hypothalamic-pituitary-adrenal axis. Proc R Soc London B: Biol Sci 2010;277:1627–33.

[55] Kim LU, D'Orsogna MR, Chou T. Onset, timing, and exposure therapy of stress disorders: mechanistic insight from a mathematical model of oscillating neuroendocrine dynamics. BMC Biol Direct 2016;11:13.

[56] Kim LU, D'Orsogna MR, Chou T. Perturbing the Hypothalamic-Pituitary-Adrenal Axis: a mathematical model for interpreting PTSD assessment tests. Computat Psychiatry 2018;2:28–49.

[57] Gillette MU, Tischkau SA. Suprachiasmatic nucleus: the brain's circadian clock. Recent Prog Horm Res 1999:33–58.

[58] Reppert SM, Weaver DR. Coordination of circadian timing in mammals. Nature 2002:1627–33.

[59] Ketema PN, Talib SB, Tosini G. The role of retinal photoreceptors in the regulation of circadian rhythms. Reviews in Endocrine Metabolic Disorders 2009;10:271–8.

[60] Herman JP, Figueiredo H, Mueller NK, Ulrich-Lai YM, Ostrander MM, Choi DC, Cullinan WE. Central mechanisms of stress integration: Hierarchical circuitry controlling hypothalamo-pituitary-adrenocortical responsiveness. Front Neuroendocrinol 2003:151–80.

[61] Watts A. Glucocorticoid regulation of peptide genes in neuroendocrine CRH neurons: a complexity beyond negative feedback. Front Neuroendocrinol 2005;26:109–30.

[62] Ono N, De Castro J, McCann S. Ultrashort-loop positive feedback of corticotropin (ACTH)-releasing factor to enhance ACTH release in stress. Proc Nat Acad Sci 1985;82:3528–31.

[63] Tsai SY, Carlstedt-Duke J, Weigel NL, Dahlman K, Gustafsson J, Tsai M, O'Malley BW. Molecular interactions of steroid hormone receptor with its enhancer element: Evidence for receptor dimer formation. Cell 1988;55:361–9.

[64] Rocsoreanu C, Georgescu A, Giurgiteanu N. The FitzHugh-Nagumo model: Bifurcation and dynamics. Boston: Kluwer Academic Publishers; 2000.

[65] Ichitovkina EG, Zlokazova MV, Solovyev AG, Kharkova OA, Shutko GV. Predicting the emergence of prenosological mental disorders in combatants. Human Ecol 2016;10:47–50.

[66] Kuhen CM, Orszag SA. Advanced mathematical methods for scientists and engineers I: Asymptotic methods and perturbation theory. New York, NY: Springer-Verlag; 1999.

[67] Souetre E, Salvati E, Belugou JL, Pringuey D, Candito M, Krebs B, Ardisson JL, Darcourt G. Circadian rhythms in depression and recovery: evidence for blunted amplitude as the main chronobiological abnormality. Psychiatry Res 1989;28:263–78.

[68] Gupta D, Morley JE. Hypothalamic-pituitary-adrenal (HPA) axis and aging. Comprehensive Physiol 2014;4:1495–510.

[69] Seeman TE, Singer B, Wilkinson CW, McEwen B. Gender differences in age-related changes in HPA axis reactivity. Psychoneuroendocrinology 2001;26:225–40.

[70] Uhart M, Chong RY, Oswald L, Lin PI, Wand GS. Gender differences in hypothalamic-pituitary-adrenal (HPA) axis reactivity. Psychoneuroendocrinology 2006;31:642–52.

[71] Simunkova K, Starka L, Hill MN, Kriz L, Hampl R, Vondra K. Comparison of total and salivary cortisol in a low-dose ACTH (synacthen) test: Influence of three-month oral contraceptives administration to healthy women. Physiol Res 2008;57:S193–9.

[72] Crowley SJ, Cain SW, Burns AC, Acebo C, Carskadon MA. Increased sensitivity of the circadian system to light in early/mid-puberty. J Clin Endocrinol Metab 2015;100:4067–73.

[73] Phillips AJK, Vidafar P, Burns AC, McGlashan EM, Anderson C, Rajaratnam SMW, Lockley SW, Caina SW. High sensitivity and interindividual variability in the response of the human circadian system to evening light. Proc Nat Acad Sci 2019;116:12019–24.

[74] Carpenter GA, Grossberg S. A neural theory of circadian rhythms: Aschoff's Rule in diurnal and nocturnal mammals. Adv Psychol 1987;42:353–85.

[75] Sateia MJ. International Classification of Sleep Disorders-Third Edition. Chest 2014;146:1387–94.

[76] Couto-Moraes R, Palermo-Neto J, Pekelmann-Markus R. The immune-pineal axis: stress as a modulator of pineal gland function. Ann N Y Acad Sci 2009;1153:193–202.

[77] Torres-Farfan C, Richter HG, Rojas-Garcia P, Vergara M, Forcelledo ML, Valladares LE, Torrealba F, Valenzuela GJ, Seron-Ferre M. Melatonin receptor in the primate adrenal gland: Inhibition of adrenocorticotropin-stimulated cortisol production by melatonin. J Clin Endocrinol Metab 2003;88:450–8.

[78] Wetterberg L. The relationship between the pineal gland and the pituitary-adrenal axis in health, endocrine and psychiatric conditions. Psychoneuroendocrinology 1983;8:75–80.

[79] Agorastos A, Nicolaides NC, Bozikas VP, Chrousos GP, Pervanidou P. Multilevel interactions of stress and circadian system: implications for traumatic stress. Front Psychiatry 2020;10:1003.

[80] Jordan D, Smith P. Nonlinear Ordinary Differential Equations: An Introduction for Scientists and Engineers. Oxford University Press; 2007.